

Modeled sensitivity of the Northwestern Pacific upper-ocean response to tropical cyclones in a fully-coupled climate model with varying ocean grid resolution

Author: Hui Li¹, Ryan L. Sriver¹, and Marlos Goes^{2, 3}

¹ Department of Atmospheric Sciences, University of Illinois at Urbana-Champaign, Urbana, IL, USA

² Cooperative Institute for Marine and Atmospheric Studies, University of Miami, Miami, FL, USA

³ NOAA/AOML, Physical Oceanography Division, Miami, FL, USA

Revised Draft for: JGR-Ocean

Draft Date: December 03, 2015

Key points:

- A high resolution Earth system model, capable of simulating realistic tropical cyclone-like circulations, is used to analyze the upper-ocean response to tropical cyclone forcing.
- High-resolution coupled model simulations demonstrate skill in simulating realistic TC-induced sea surface responses and upper ocean heat convergence.
- Results indicate that TCs can influence upper-ocean mixing and heat budgets, potentially leading to climate feedbacks affecting large-scale ocean/atmosphere circulation patterns and transports.

22

23

Abstract:

24 Tropical cyclones (TCs) actively contribute to Earth's climate, but TC-climate
25 interactions are largely unexplored in fully-coupled models. Here we analyze the upper-
26 ocean response to TCs using a high resolution Earth system model, in which a 0.5°
27 atmosphere is coupled to an ocean with two different horizontal resolutions: 1° and 0.1° .
28 Both versions of the model produce realistic TC climatologies for the northwestern
29 Pacific region, as well as the transient surface ocean response. We examined the potential
30 sensitivity of the coupled modeled responses to ocean grid resolution by analyzing TC-
31 induced sea surface cooling, latent heat exchange and basin-scale ocean heat
32 convergence. We find that sea surface cooling and basin-scale aggregated ocean heat
33 convergence are relatively insensitive to the horizontal ocean grid resolutions considered
34 here, but we find key differences in the post-storm restratification processes related to
35 mesoscale ocean eddies. We estimate the annual basin-scale TC-induced latent heat
36 fluxes are $1.70 \pm 0.16 \cdot 10^{21}$ J and $1.43 \pm 0.16 \cdot 10^{21}$ J for the high-resolution and low-
37 resolution model configurations, respectively, which account for roughly 45% of the total
38 TC-induced ocean heat loss from the upper ocean. Results suggest that coupled modeling
39 approaches capable of capturing ocean-atmosphere feedbacks are important for
40 developing a complete understanding of the relationship between TCs and climate.

41

1. Introduction:

Increasing evidence suggests TCs play an active role in influencing the dynamics of the coupled ocean-atmosphere system [Emanuel, 2001; Hart, 2011; Sriver *et al.*, 2008, 2010; Sriver and Huber, 2007]. Several recent studies have shown that enhanced upper ocean mixing, associated with extreme TC winds, could lead to positive ocean heat convergence (OHC) [Bueti *et al.*, 2014; Emanuel, 2001; Jansen *et al.*, 2010; Mei *et al.*, 2013, p.m; Mei and Pasquero, 2012; Park *et al.*, 2011; Sriver, 2013; Sriver *et al.*, 2010; Sriver and Huber, 2007], which may potentially alter large-scale circulations and transports of the ocean-atmosphere system [Boos *et al.*, 2004; Emanuel, 2001; Hu and Meehl, 2009; Jansen and Ferrari, 2009; Pasquero and Emanuel, 2008; Sriver and Huber, 2010]. These TC processes and feedbacks are not generally captured in current numerical models used for climate projections, but their representation may be necessary to reduce uncertainty in projections of climate change impacts.

Numerical models are useful tools to explore the relationship between TCs and climate. Many uncoupled atmosphere and ocean modeling experiments have pointed to important climate connections associated with TCs. High resolution atmosphere models have demonstrated skill in simulating realistic TC-like circulations and basin-scale climatologies, and they have been used to examine the sensitivity of TC activity to prescribed changes in climate [Bacmeister *et al.*, 2013; Camargo *et al.*, 2005; Wehner *et al.*, 2010], and increasing atmosphere model grid resolution can significantly improve the representation of simulated TCs [Bacmeister *et al.*, 2013; Li *et al.*, 2013; Manganello *et al.*, 2012; Murakami and Sugi, 2010; Strachan *et al.*, 2012; Walsh *et al.*, 2013; Wehner *et*

65 *al.*, 2014]. In addition to atmosphere-only experiments, ocean-only models have been
66 used extensively to analyze the oceanic response to TC forcing, including TC influences
67 on ocean heat convergence [*Jansen and Ferrari*, 2009; *Vincent et al.*, 2013], mixing
68 budgets [*Huang et al.*, 2009; *Mei and Pasquero*, 2012], and large-scale ocean heat
69 transport and circulations [*Bueti et al.*, 2014; *Jansen and Ferrari*, 2009; *Jullien et al.*,
70 2012; *Sriver et al.*, 2010; *Sriver and Huber*, 2010; *Vincent et al.*, 2013; *Wang et al.*,
71 2014].

72
73 Ocean-atmosphere coupling is important for quantifying surface fluxes of heat and
74 momentum within storm-affected regions [*Bender and Ginis*, 2000; *Jullien et al.*, 2014],
75 as well as potential remote impacts associated with altered dynamics [*Bender and Ginis*,
76 2000; *Jullien et al.*, 2014; *Pasquero and Emanuel*, 2008; *Scoccimarro et al.*, 2011].
77 Several recent modeling studies have shown that coupled climate models are capable of
78 simulating present day TC statistics, including geographical distribution, frequency and
79 interannual variability [*Bell et al.*, 2013; *Gualdi et al.*, 2008; *Kim et al.*, 2014; *Rathmann*
80 *et al.*, 2014]. These models typically exhibit biases across different basins due to their
81 generally coarse model resolution, relatively short simulation times, and/or uncertainties
82 related to integrated model responses and interactions. Coupled climate models have also
83 been used to explore potential TC connections to large-scale climate features. For
84 example, *Hu and Meehl* [2008] use a relatively coarse resolution ($\sim 2.8^\circ$ atmosphere $\sim 1^\circ$
85 ocean) version of the Community Climate System Model (CCSM), to explore the effect
86 of TCs on meridional volume and heat transports, finding that the positive influence of
87 TC-induced diapycnal ocean mixing on meridional transports is partially modulated by

increased freshwater forcing associated with heavy TC precipitation. Also using a relatively low resolution version of CCSM3, *Manucharyan et al.* [2011] analyzed how imposed intermittent vertical ocean mixing associated with TC events may affect large-scale ocean temperature structure and circulation patterns. They found that the additional TC-like mixing leads to both enhanced poleward ocean heat transport and tropical equatorial heat convergence. *Scocccimano et al.* [2011] investigated the North Hemisphere poleward ocean heat transport induced by model-generated TCs on both transient and long-term time scales with a 0.75° atmosphere and 2° ocean. They concluded that TCs could largely enhance the ocean heat transport on weekly time scales, but the effect is negligible when considering annually averaged ocean heat transport.

These past studies have provided fundamental insights into the potential relationship between TCs and climate, but they are generally limited by relatively coarse ocean grid resolution and a lack of appropriate ocean-atmosphere coupling for analyzing TC effects in the coupled system. While several studies (e.g. Wehner et al., 2014) have investigated the effects of increased atmosphere resolution on TC climatologies, the sensitivity of the upper-ocean response to ocean grid resolution has not been adequately addressed within coupled model frameworks. Here we analyze the upper ocean response to TCs using a high-resolution configuration of the Community Climate System Model version 3.5 (CCSM 3.5) [*Kirtman et al.*, 2012], which features an atmosphere model with 0.5° horizontal resolution coupled to an ocean model with two different horizontal resolutions (1° and 0.1°). This model is capable of simulating realistic TC circulations and cold wakes (Figure 1), as well as TC-induced subsurface thermocline warming [*McClean et*

al., 2011]. We use the results of the model experiments to analyze TC climatologies, the transient upper ocean response to TC passage, and basin-scale aggregated TC effects on ocean heat convergence and surface heat fluxes. We focus our analysis on the Northwestern Pacific Ocean, which represents a region exhibiting a realistic TC climatology and seasonal variability within both model configurations. A key goal of this paper is to examine the potential sensitivity of the coupled modeled response to increasing ocean grid resolution towards scales capable of resolving mesoscale ocean eddies.

This paper is organized as follows. Section 2 describes the model, observational data, TC tracking scheme and methods for the OHC calculations. Section 3 is the main results section, which is divided into three parts. We first analyze and compare the modeled TC climatologies of the two model configurations. We then investigate the sensitivity of surface responses, including surface cooling and latent heat fluxes, to ocean grid resolution. In particular, the sensitivities are further examined by analyzing potential effects of parameterized versus resolved mesoscale ocean eddies. Lastly, we show first-order estimates of the basin-scale annual mean TC-induced latent heat budget and ocean heat convergence within the coupled model. The caveats of this study are discussed in Section 4. The main conclusions and implications of this work are summarized in Section 5.

2. Data and Methods:

2.1 Model description

We analyze model output from a set of century-scale present-day control simulations using high-resolution configurations of CCSM 3.5 [Gent *et al.*, 2010; Kirtman *et al.*, 2012; McClean *et al.*, 2011]. CCSM3.5 is a pre-release version of CCSM4 and includes the Community Atmospheric Model (CAM) version 3.5 [Gent *et al.*, 2010; Neale *et al.*, 2008] coupled to the Parallel Ocean Program (POP) version 2 [Danabasoglu *et al.*, 2012; Gent *et al.*, 2010]. The modeling experiment consists of two simulations in which the 0.5° atmosphere component model is coupled to two different versions of the ocean model. The low-resolution control simulation features ocean and sea-ice components with a nominal 1° horizontal resolution, with constant grid spacing in the zonal direction (1.2°) and varying grid spacing in the meridional direction (0.27° at the equator to 0.54° in the mid-latitudes). The high-resolution control simulation features ocean and sea-ice components with a uniform 0.1° horizontal spacing at the equator, and reducing to ~0.02° at high latitudes. Both ocean model versions have 42 vertical levels with thickness varying from 10 m at the surface to 250 m at 6000 m depth. Momentum and heat fluxes at the air-sea interface are computed by the coupler and are shared among model components. Surface wind stress is calculated using relative wind, which refers to the difference between lowest model level wind and ocean current velocities. Ocean vertical mixing is parameterized using K-profile parameterization (KPP) scheme. Kirtman *et al.* [2012] find that small scale features resolved in the high resolution ocean model (e.g. mesoscale eddies) can alter large scale climate conditions, such as global mean temperature, general circulation patterns, Arctic sea ice losses, rainfall, ocean stratification, climate variability and air-sea interactions.

The simulations include over 100 years of monthly output from the ocean and atmosphere models, of which roughly 20 years of output also include a subset of daily surface variables. We focus our analysis primarily on the 20 years of daily surface output for analyzing the transient TC effects. Available daily variables from the model simulations include: surface wind stress, surface temperature, surface latent and sensible heat fluxes, and precipitation rate. The daily model output does not contain any subsurface ocean variables. Our analysis is limited by the lack of daily subsurface ocean information; however, the available atmosphere surface outputs enable us to perform comprehensive sensitivity analyses of the transient TC-induced responses near the ocean-atmosphere interface. In addition, we analyze basin-scale TC-induced ocean heat budgets using previously published methods that combine daily surface temperature information with monthly vertical temperature profiles [Sriner *et al.*, 2008] (see Section 2.4), which are available for these simulations. These methods have been shown to provide robust first-order estimates of transient ocean heat uptake compared to altimetry-based estimates [Mei *et al.*, 2013]. Note that such methods may overestimate the ocean heat uptake considering the importance of the variations in the pre-storm stratification [Vincent *et al.*, 2012b], vertical advection [Jullien *et al.*, 2012] and thermocline seasonal variations [Jansen *et al.*, 2010]. These limiting assumptions provide important constraints on the first-order estimates of surface fluxes and ocean heat convergence.

2.2 Tropical cyclone detection and tracking algorithm

We developed an algorithm to identify TC-like circulations in the model. The algorithm is adapted from previous studies analyzing TCs in atmosphere-only simulations

[Camargo and Zebiak, 2002; Li et al., 2013; Walsh et al., 2007; Zhao et al., 2009], based on the availability of daily variables outlined in Section 2.1. We identify a TC-like circulation within the model using the following criteria: (1) cyclogenesis occurs within 30° of the equator; (2) the maximum surface wind stress curl exceeds $2 \cdot 10^{-6} \text{ N} \cdot \text{m}^{-3}$, and maximum 10m wind speed exceeds $15 \text{ m} \cdot \text{s}^{-1}$ corresponding to a relaxed threshold for the minimum wind speed for a tropical storm; (3) the horizontal scale is larger than 200 km; (4) the storm center must not be stationary for more than 24 hours; and (5) the event must last for at least 3 days. Criteria (3) and (4) are important constraints to filter standing ocean eddies, since we are using relative wind (differences between 10 m wind and ocean current) derived from surface wind stress as the basis for constructing TC surface wind fields. Several of our criteria are consistent with previous TC detection methods [Camargo and Zebiak, 2002; Zhao et al., 2009], however, some differences are necessary given the limited number of variables available from the model output. For example, maximum surface wind stress curl is used to identify and locate a potential TC storm center, rather than the 850 hPa vorticity and minimum sea level pressure. In addition, the cyclone core structure is not considered here. We have performed multiple sensitivity tests to optimize the detection and tracking algorithms and we calibrate the threshold values for each variable. Results are visually inspected to ensure the characteristics of the identified circulations are consistent with TC events (Figure 1). Additional details about the procedure can be found in the supplementary material.

2.3 Observational data

202 We use the Optimally Interpolated Sea Surface Temperature (OI SST) data product to
203 analyze observed TC-induced near-surface ocean temperature responses. The OI SST is a
204 hybrid product of the Tropical Rainfall Measuring Mission's (TRMM) Microwave
205 Imager (TMI) and the Advanced Microwave Scanning Radiometer (AMSRE) data, which
206 provides complete daily SST at 0.25° horizontal resolution from 2002 to present
207 [Gentemann, 2003, 2004; Gentemann *et al.*, 2010]. We analyze all TCs globally between
208 2003 and 2012 as defined by the best track data set, which combines track information
209 from NOAA's Storm Prediction Center and the U.S. Navy's Joint Typhoon Warning
210 Center. The best track product categorizes TC tracks within five different regions: North
211 Atlantic, East Pacific, West Pacific, Indian Ocean, and Southern Hemisphere. We analyze
212 sub-surface ocean properties using potential temperature profiles and mixed layer depths
213 from the European Center for Medium-Range Weather Forecast Ocean Reanalysis
214 System 4 (ECMRWF ORAS4), providing monthly ocean state information between 1957
215 and present. Climatological mixed layer depth and SST in ORAS4 are compared with
216 that from the World Ocean Atlas 2013 (WOA13) [Locarnini *et al.*, 2013] to ensure
217 validity of this dataset (Supplementary Figures S5 - S8). Annually and seasonally
218 averaged observational wind data is from National Center for Climate Prediction/
219 National Center for Atmospheric Research (NCEP/NCAR) reanalysis. Monthly averaged
220 eddy kinetic energy (EKE) is derived from 17 years (1993~2010) of monthly averaged
221 sea surface height anomalies (SSA) [Le Traon *et al.*, 1998], produced by Ssalto/Duacs
222 and distributed by Aviso. The data is a gridded 1/4 ° x 1/4 ° global product merged from
223 several altimeter satellite missions. The sea level anomalies are referenced to a 20-year
224 period (1993-2012).

2.4 Calculation of TC-induced ocean heat convergence (OHC)

The TC-induced, vertically integrated OHC is estimated following previous methods [Emanuel, 2001; Srivier *et al.*, 2008; Srivier and Huber, 2007][Emanuel, 2001; Srivier and Huber, 2007; Srivier *et al.*, 2008]:

$$OHC = \iiint F \Delta T dh dW dL \quad (1)$$

where F is the fraction of heat transported downward through the base of the oceanic mixed layer through mixing and entrainment, ΔT is the magnitude of surface temperature anomaly, dh is the depth of vertical mixing, and dW and dL are the cross-track and along-track length of the storm wake. Seawater density ρ and heat capacity C are held constant at 1020 kg/m^3 and $3900 \text{ J/(kg} \cdot ^\circ\text{C)}$, respectively. In order to estimate F , we analyze surface latent heat exchange during TC days, as it is the second largest contributor to sea surface cooling [Huang *et al.*, 2009] (see Section 3.3). We employ a footprint method that samples surface properties within a $6^\circ \times 6^\circ$ domain (dW and dL), which is centered on the best track location and moves with the storm. The footprint domain size is consistent with area sizes used in other studies [Cheng *et al.*, 2014; Hart *et al.*, 2007; Lloyd and Vecchi, 2011; Mei and Pasquero, 2012; Srivier *et al.*, 2008; Srivier and Huber, 2007]. At each storm location, temperature anomalies are calculated using SST from 2 days after storm passage relative to the average SST between 12 and 5 days prior to the storm. Sensitivity analyses were performed to choose characteristic sizes of the footprint domain and time interval, and we chose values that maximized the TC effect. The results presented here are generally insensitive to the choice of spatial and

temporal sampling scales, particularly for the comparison between model simulations with varying ocean grid resolution.

We use three different strategies for estimating TC-induced mixing depths that we apply to both model simulations and observations. First, we assume a uniform and constant mixing depth of 50m, consistent with past case study analysis [D'Asaro *et al.*, 2007] and methods used in previous observation-based studies [Sriner and Huber, 2007]. For the second method, we assume that vertical mixing for all storms penetrates to levels corresponding to the monthly climatological mixed layer depth at each grid point. In the third method, we combine the TC-induced SST anomalies with monthly climatological vertical ocean temperature profiles to estimate mixing depth as the level from which water must be upwelled to achieve the observed surface temperature anomaly [Sriner *et al.*, 2008]. In this method, mixing depth is calculated as $dh = \Delta T \cdot \partial z / \partial T$, where ΔT is the TC-induced SST anomaly and $\partial z / \partial T$ is the inverse of the vertical temperature gradient obtained from the monthly climatological ocean temperature at each location. All three methods likely under-estimate the actual TC-induced vertical mixing length scale, but we chose these criteria in order to examine the robustness of the model's response and resolution dependence under uncertain assumptions. Ocean heat convergence on each grid point is then calculated individually before being integrated across the footprint domain, to account for any non-uniform cooling anomalies within the domain.

3. Model Results and Discussion

3.1 Modeled tropical cyclone number and climatology

TC tracks accumulated over 20 years in both versions of the model are shown in Figure 2a and 2b. We find that both the low-resolution and high-resolution simulations generally capture the spatial distribution of the global storm tracks. However, both model configurations exhibit several key limitations. The total number of storms globally is roughly 50 % of the observed current-day climatology (Table 1). The annual TC counts in the north Atlantic and east Pacific basins are too low compared to observed climatologies (Figure 3). For the north Atlantic region, the bias may be attributed to relatively low annual SST (Supplementary Figure S1) and relatively high vertical wind shear (Supplementary Figure S2) within the Main Development Region for both simulations, which are both important environmental factors for TC development. The model also simulates storms in the South Atlantic basin, which are rarely observed in nature. The cause may be due to anomalously low vertical wind shear and warm SST in this region compared to observations (Supplementary Figures S1 and S2).

In addition, the model does not capture storm intensities greater than Category 3 (Figure 2). The storm intensity distributions are similar between the two versions of the model, and they are shifted towards low values compared to observations (Figure 4). The biases in intensity and number are likely linked to the relatively coarse (0.5°) atmosphere component resolution [Li *et al.*, 2013; Shaevitz *et al.*, n.d.; Strachan *et al.*, 2012; Zhao *et al.*, 2009], and similar limitations are common among other Earth system models [Camargo, 2013]. Recent findings using newer versions of CAM with higher horizontal grid resolution (0.25°) show significant improvements in the total number, although

biases still exist in the storm intensity and spatial distribution [Bacmeister *et al.*, 2013; Wehner *et al.*, 2014]. The intensity bias may also be due to the different methods of computing daily averaged storm wind speed between observations and model output. The best-track daily wind product represents the average of the 6-hourly instantaneous maximum winds. The daily wind from the model is averaged over the entire day given the daily ocean model output frequency, which would smooth out the peak wind speed and lead to a low-bias compared to averages of 6-hourly instantaneous winds. To test the hypothesis that the wind bias is due to the differences in time-averaging, we analyzed 5 years of storm intensity distributions using a separate high resolution (0.25 deg. atmosphere, 0.1 deg. ocean) CESM coupled simulation [Small *et al.*, 2014] where daily and 6-hourly output frequencies are both available for the same time period. We found that while the intensity distribution from the 6-hourly output is quite consistent with observations, the distribution computed from the daily output exhibits a similar low bias to our current model analysis (Supplementary Figure S3). This suggests that climate models with 6-hourly output frequency exhibit more accurate TC intensity distributions when comparing model output with best track data. Despite these biases, we find the CCSM3.5 model captures the observed seasonal variability in several key basins (see Figure 3), including the Northwestern Pacific region, which is where we focus our analysis.

The consistency in storm intensity distribution suggests that both versions of the model represent similar climatological environmental conditions important for TC intensity. The effect of pre-storm SST is of particular interest here, since it may be sensitive to the

representation of mesoscale eddies. In order to diagnose the sensitivity of pre-storm SST to model resolution, we analyzed the frequency distribution of SST anomalies 3 days prior to storm passage for all storm days (Supplementary Figure S4). The anomalies are referenced to daily climatological values. The results show no significant difference in the distributions, suggesting that eddies do not have a major impact on pre-storm SST conditions in the model.

3.2 Modeled TC-induced sea surface responses

3.2.1. Spatial and temporal characteristics of sea surface cooling

The annual averages of the accumulated TC-induced temperature anomalies for each version of the model are shown in Figure 2c and 2d. Both model versions exhibit spatial patterns of cooling that are consistent with previous observation-based analyses [Srивer *et al.*, 2008; Srивer and Huber, 2007]. The magnitude of the accumulated TC-induced surface cooling in the model is generally lower compared to observations, which is due primarily to the model's under-representation of the TC number and intensity. In addition, the modeled surface temperature response is generally insensitive to horizontal ocean grid resolution, and the biases are minimal in the Northwestern Pacific region.

In order to diagnose the transient response of upper ocean temperature to TC passage, we analyze time series composites of the area-averaged SST anomalies for the low-resolution and high-resolution simulations (Figure 5). The anomalies are referenced to the pre-storm conditions (Figure 5, right panel), which are defined as the average SST over 12 to 5 days before the storm arrival, as well as to the 20-year daily climatology

(Figure 5, left panel). Comparing against climatologies can be useful to remove seasonal effects on timescales longer than a few weeks. We test the sensitivity of the SST response to the averaging domain size using multiple footprints ($2^\circ \times 2^\circ$, $6^\circ \times 6^\circ$, $10^\circ \times 10^\circ$). In both model simulations, SST begins to decrease 2-3 days prior to the storm arrival, and it reaches a minimum 2 days following passage of the storm center. The magnitude of the maximum cooling is generally consistent between the two configurations. However, the high resolution configuration shows cooling approximately 0.1°C stronger than the low resolution configuration within the $2^\circ \times 2^\circ$ averaging footprint size, which may be due to differences in horizontal advection or surface heat fluxes (discussed in Section 3.2.2). This difference is smoothed out when averaged over a larger area. In both versions of the model, the time scales of SST restoration to climatologically normal conditions are much longer than suggested by the observations [*Dare and McBride*, 2011; *Lloyd and Vecchi*, 2011; *Mei and Pasquero*, 2012]. In the high resolution configuration, SST returns to climatology about 120 days later; in the low resolution configuration, the cold anomaly persists even after 200 days, which is similar to recent results of an ocean-only modeling experiment [*Jullien et al.*, 2012].

3.2.2 Temporal evolution of surface latent heat exchanges

The temporal evolution of the surface latent heat fluxes during storm passage is shown in Figure 6. Similar to the analyses of the surface cooling, we averaged the latent heat fluxes using different footprint sizes centered on the TC center. Latent heat fluxes are represented as total values (Figure 6, right panel), as well as anomalies referenced to the long-term-mean daily climatology (Figure 6, left panel). In both versions of the model,

latent heat fluxes begin to increase about a week before the storm's arrival, indicating an anomalous heat supply from the ocean to the atmosphere prior to the storm. The coupled model shows a spike on the day of the storm passage, and the peak value of the daily heat fluxes in the high resolution version is slightly higher than its low resolution counterpart across all the footprint sizes.

Using the $6^\circ \times 6^\circ$ footprint domain, we find the long term mean climatological daily average latent heat fluxes without TC forcing is $158 \text{ W} \cdot \text{m}^2$ ($145 \text{ W} \cdot \text{m}^2$) in the high (low) resolution ocean configuration, while the latent heat flux under TC conditions is $270.61 \text{ W} \cdot \text{m}^2$ ($241.75 \text{ W} \cdot \text{m}^2$) in the high (low) resolution configuration. The magnitudes of latent heat fluxes with and without TCs are both consistent with the observational estimates based on Hurricane Isabel using high resolution satellite-derived dataset [Liu *et al.*, 2011]. We use an observation-based case study of the Category 4 hurricane Frances in 2004 [Huang *et al.* 2009], as a first-order constraint on the modeled fluxes. Huang *et al.* [2009] estimate the daily averaged latent heat fluxes aggregated over a 400 km area on the day of the maximum intensity is 0.09 PW. In the current study, the two strongest daily-averaged storm winds are $50 \text{ m} \cdot \text{s}^{-1}$ in low resolution version and $50.3 \text{ m} \cdot \text{s}^{-1}$ in high resolution version. Since the daily-averaged wind would underestimate the storm intensity (for reasons discussed in Section 3.1), it is possible that instantaneous winds may reach Category 4 (sustained wind $>58 \text{ m} \cdot \text{s}^{-1}$). The corresponding latent heat flux peak values integrated over a 400 km area are 0.12 PW and 0.14 PW, which are on the same order with the estimate of Huang *et al.* [2009].

The model also captures the reduction of latent heat fluxes caused by the cold wake after TC passage. The fluxes decrease by $\sim 30 \text{ W} \cdot \text{m}^2$ when averaged over the 2° area and $\sim 20 \text{ W} \cdot \text{m}^2$ when averaged over the 6° area, representing $\sim 13\%$ to 20% decrease compared to the pre-storm values. The reduction in latent heat fluxes is consistent with observation-based studies [D'Asaro *et al.*, 2007; Liu *et al.*, 2011], indicating that the coupled model approaches with a dynamic ocean may be capable of realistically capturing the negative feedbacks on TC intensification missing from atmosphere-only simulations.

3.2.3 Potential modeled effects of mesoscale ocean eddies on TC wake recovery

Horizontal ocean grid resolution may be important for simulating the storm-scale transient dynamic responses. In particular, the upper ocean restratification following TC wakes may be influenced by mesoscale eddy transport and mixing [Haney *et al.*, 2012]. Mesoscale eddies' horizontal scales are of the order of the baroclinic Rossby radius of deformation, typically of $O(10\text{km})$ (e.g., Killworth *et al.*, 1997; Chelton *et al.*, 1998). These effects are largely parameterized in the 1° version of the model and explicitly resolved in the 0.1° model.

To explore the effect of mesoscale eddies on the TC-induced upper ocean response, we analyzed TC activity within regions of high and low annual mean eddy kinetic energy (EKE) for both models and satellite-based observations [Le Traon *et al.*, 1998]. We estimate EKE using monthly sea surface height anomalies (SSHA) in both the observational data and model output. The global annual mean EKE for the model

simulations and observations are shown in Figure 7. Both versions of the model generally capture the spatial distribution of EKE, but the 0.1° model exhibits substantial improvement in the magnitude of EKE compared to the 1° ocean model (see also [Maltrud and McClean, 2005; McClean *et al.*, 2002; Smith *et al.*, 2000]).

We first examine the potential relationship between wake recovery and background EKE by analyzing average wake responses within a high EKE region ($30^\circ - 40^\circ$ N, $130^\circ - 175^\circ$), corresponding to large eddy activity within the Kuroshio current and extension. We analyzed the time series composites of the area-averaged ($2^\circ \times 2^\circ$) SST anomalies and their e-folding recovery time scales, which is defined as the number of days necessary for the SST anomaly to return to e^{-1} of the maximum cooling (Figure 8). The two model versions exhibit similar characteristics, including the fluctuating pattern of SST time series, the magnitudes of maximum cooling, and the e-folding time scales of 13 days.

We performed further analyses regarding the relationship between EKE, SST cooling and e-folding time by including all the storm days globally, in an attempt to gain additional insight into the sensitivity of the responses to ocean grid resolution. Figure 9 shows the relationship between EKE and e-folding time (upper), and between EKE and maximum SST cooling (lower). EKE is normalized in the right panels, in which the circles are bin averages and the error bars are their respective standard errors. Results indicate that, although the EKE magnitudes are very different between the model simulations and observations, the TC-induced responses exhibit similar patterns when using normalized

EKE. In particular, the e-folding time in the high EKE regions are generally consistent between observations and the 0.1° ocean simulation, suggesting the potential importance of eddies in wake recovery and possible improvement of the 0.1° ocean model over the 1° model. However, the relevance and robustness of this result is difficult to interpret given the disparity in the magnitude of EKE between model simulations and lack of subsurface ocean information from the model output.

3.3 First-order estimates of TC-induced upper ocean energy budget

Despite the lack of subsurface ocean fields, the availability of daily surface properties and monthly subsurface ocean temperature enables us to estimate the modeled basin-scale TC-induced OHC using different strategies accounting for mixing depth (discussed in Section 2.4). The results are summarized in Figure10. The average TC mixing depths and their corresponding OHC estimates are sensitive to the choice of vertical mixing length scale calculation; however, the modeled OHC estimates are generally consistent between the two simulations for each mixing depth calculation. Differences between the two simulations may be partly attributed to variations in the background ocean state (Supplemental Figure S4), since the upper ocean temperature structure in the high-resolution model exhibits stronger stratification effects than the low resolution model. We find that varying mixing depths based on the climatological vertical ocean temperature gradients leads to the largest estimation of TC-induced OHC. This is because the location of the most significant surface cooling corresponds to areas with the deepest mixing, as indicated by the large spread over the mean mixing depth for this method (Figure10a). In

contrast, defining the mixing length based on the depth of the climatological mixed layer yields the smallest TC-induced OHC. This method likely underestimates the effect of TCs on the vertical redistribution of ocean heat, even for relatively low intensity storms considered here, because TC-induced mixing typically penetrates to depths significantly below the base of the seasonal mixed layer.

In addition to vertical mixing, TC-induced latent heat fluxes can also contribute to ocean surface cooling. Coupled modeling frameworks have the advantage of capturing surface fluxes within TC regions. We have shown in Section 3.2.2 that both versions of the model are capable of simulating surface latent heat responses to TCs that are generally consistent with observations. Here we estimate the basin-scale annually accumulated TC-induced latent heat budget within the coupled model and its contribution to the total upper ocean heat loss during TC passage.

For each storm day, we integrate the daily average latent heat fluxes from day 0 to day 2 relative to TC passage over a 6° domain. The period of 0-2 days is chosen in order to account for all the latent heat exchange responsible for the total upper ocean heat loss, which we estimate with the maximum SST cooling that occurs on day 2 (see Figure 5). The annually accumulated basin-scale latent heat fluxes are $1.70 \pm 0.16 \cdot 10^{21}$ J in the high resolution model and $1.43 \pm 0.13 \cdot 10^{21}$ J in the low resolution model, representing 47% and 45% of the total TC-induced OHC estimates in the high and low resolution model configurations, respectively (see also Table 2). This contribution of latent heat exchange is similar to the estimate of Vincent et al. [2012a], who found ~43% of ocean

heat anomalies are due to latent heat fluxes. Results suggest that surface latent heat fluxes account for a substantial amount of heat loss from the upper ocean during TC events, which may have important implications for global heat and energy budgets in coupled models.

We apply the basin-scale latent heat flux as a constraint on the oceanic heat convergence induced by TCs in the model simulations (corresponding to $F=0.53$ (0.55) in the high (low) resolution version in Equation 1). Using the varying mixing depth strategy, we estimate the modeled TC-induced, surface flux-corrected annual Northwestern Pacific basin-scale OHC to be $0.17 \cdot 10^{22} \text{J}$ in the low-resolution simulation and $0.19 \cdot 10^{22} \text{J}$ in the high-resolution simulation, corresponding to a mean annual rate of $0.05 \pm 0.005 \text{ PW}$ ($1 \text{ PW}=10^{15} \text{ W}$) and $0.06 \pm 0.005 \text{ PW}$, respectively. In order to make a comparison between the model and observations, we compare the model results with 60% of the total basin-scale OHC in the observations, since the TC number in the model is about 60% of the observational record in the northwestern Pacific basin (see Table 1). Due to the lack of observational estimates of latent heat fluxes within TCs, we apply $F = 0.55$ from the model for the observational OHC calculation. The annual surface flux-corrected basin-scale OHC for all the storm intensities in the observations is $0.35 \cdot 10^{22} \text{J}$, and 60% of which is $0.21 \cdot 10^{22} \text{J}$. This value is comparable with the modeled results. These first-order estimates suggest that the coupled model is capable of capturing realistic surface heat fluxes and the upper ocean heat convergence responses to tropical cyclones. These preliminary results point to the potential importance of using high-resolution coupled modeling approaches to advance our understanding about tropical cyclones and climate.

4. Caveats

This study includes several important simplifying assumptions and caveats, in addition to the methodological constraints discussed in section 2. Although the 0.5° resolution atmosphere model is shown to be capable of capturing realistic TC circulations and spatial distributions in the northwestern Pacific, the storm intensities are likely to be underestimated. Thus, potential differences in the storm-induced responses for extremes storms cannot be examined using this model.

Shear instability induced by near-inertial waves contributes to TC-induced SST cooling through turbulent entrainment at the base of the mixed layer [Cuypers *et al.*, 2013; Ginis, 2002]. This effect is dependent on the magnitude of near-inertial energy input by the winds to the ocean, as well as the dissipation of the near-inertial energy beneath the oceanic boundary layer. The modeled near-inertial energy input by the winds is highly dependent on the resolution of the atmospheric component and on the coupling frequency [Jiang *et al.*, 2005; Jochum *et al.*, 2013]. The atmospheric model considered here (0.5°) is not capable of simulating extreme TC events or the fine-scale atmospheric frontal features that can be important for generating near-inertial energy input to the ocean. Under this situation, the KPP vertical mixing parameterization scheme used in the model would not provide sufficient near-inertial wave-induced shears [Large *et al.*, 1994; Jochum *et al.*, 2013]. A parameterization for the dissipation of near-inertial energy in the upper ocean is not applied in the present (CCSM3.5) or in more recent versions of this model [Jochum *et al.*, 2013]. Improved representation of this effect could impact mixed layer depth, SST and precipitation patterns [Jochum *et al.*, 2013]. Whether the results

presented here would change under improved representation of near-inertial waves in the model is an open question, which will be the topic of a future paper.

The effect of mesoscale eddies on ocean surface cooling due to entrainment would also likely depend on the vertical resolution. Both simulations feature the same relatively coarse vertical resolution (42 levels). Increasing vertical resolution (particularly near the surface) may induce a stronger eddy effect on surface cooling that are not captured here.

5. Conclusions

Upper ocean responses to TCs in a fully-coupled Earth system model with varying horizontal ocean grid resolution are investigated in this paper. We analyzed the resolution-dependent responses by examining simulated TC climatologies, sea surface cooling responses and latent heat budgets. We estimate TC-induced OHC in the Northwestern Pacific for both model configurations from near-surface atmosphere and ocean fields using multiple strategies accounting for uncertainties in vertical mixing length scales.

Results indicate that the ocean surface responses and basin-scale aggregated TC influences on upper-ocean heat budgets within the coupled model configurations considered here are relatively insensitive to the choice of ocean grid resolution, when considering 1° versus 0.1° resolution. This suggests that the surface eddy flux parameterization in the low-resolution model may be sufficient for capturing the basin-scale horizontal temperature distribution and heat transport induced by mesoscale eddies

[*Danabasoglu et al.*, 2008]. However, it is important to consider limitations in the ocean model's representation of near-inertial wave response when interpreting these results, as well as relatively coarse (0.5°) atmosphere model resolution which is unable to simulate frontal systems important for near-inertial energy input to the ocean. TC-induced ocean sensitivities to horizontal grid resolution may emerge with improved representation of near inertial waves, which could influence transient intra-seasonal dynamic responses to TC forcing as well as post-storm wake recovery, ocean heat uptake, upper-ocean currents, and meridional transports.

Given the magnitude of the modeled and observed TC-induced fluxes of heat and momentum at the atmosphere-ocean interface, and the resulting positive ocean heat convergence, these results point to the importance of coupled model approaches to developing a more complete understanding about the relationship between TCs and climate. Coupled modeling initiatives utilizing ultra-high resolution modeling frameworks may provide fundamental insight to potential TC-induced feedbacks that influence large-scale ocean and atmosphere heat budgets and circulation patterns.

Acknowledgement

We thank Ben Kirtman for providing the model output for the analyses in this study. Marlos Goes was partly supported by NOAA/AOML and the NOAA Climate Program Office. We also thank Kerry Emanuel for providing global TC best track data:

<http://eaps4.mit.edu/faculty/Emanuel/products>. The OI SST product is from the Remote Sensing System website (<http://www.remss.com/>), and is sponsored by National Oceanographic Partnership Program (NOPP), the NASA Earth Science Physical Oceanography Program, and the NASA MEaSUREs DISCOVER Project. The ORAS4 ocean reanalysis data is provided by the Asia-Pacific Data-Research Center of the International Pacific Research Center, which can be found on their website at <http://apdrc.soest.hawaii.edu/data/data.php>. The WOA13 product is provided by NOAA National Oceanographic Data Center. The wind shear climatology is from NCEP Reanalysis, which is provided by the NOAA/OAR/ESRL PSD, Boulder, Colorado, USA, from their Web site at <http://www.esrl.noaa.gov/psd/>. The altimeter products were produced by Ssalto/Duacs and distributed by Aviso with support from Cnes.

References

- Bacmeister, J. T., M. F. Wehner, R. B. Neale, A. Gettelman, C. Hannay, P. H. Lauritzen, J. M. Caron, and J. E. Truesdale (2013), Exploratory High-Resolution Climate Simulations using the Community Atmosphere Model (CAM), *J. Clim.*, 27(9), 3073–3099, doi:10.1175/JCLI-D-13-00387.1.
- Bell, R., J. Strachan, P. L. Vidale, K. Hodges, and M. Roberts (2013), Response of Tropical Cyclones to Idealized Climate Change Experiments in a Global High-Resolution Coupled General Circulation Model, *J. Clim.*, 26(20), 7966–7980, doi:10.1175/JCLI-D-12-00749.1.
- Bender, M. A., and I. Ginis (2000), Real-case simulations of hurricane-ocean interaction using a high-resolution coupled model: Effects on hurricane intensity, *Mon. Weather Rev.*, 128(4), 917–946.

593 Boos, W. R., J. R. Scott, and K. A. Emanuel (2004), Transient Diapycnal Mixing and the
 594 Meridional Overturning Circulation, *J. Phys. Oceanogr.*, *34*(1), 334–341,
 595 doi:10.1175/1520-0485(2004)034<0334:TDMATM>2.0.CO;2.

596 Buetti, M. R., I. Ginis, L. M. Rothstein, and S. M. Griffies (2014), Tropical Cyclone-
 597 Induced Thermocline Warming and its Regional and Global Impacts, *J. Clim.*,
 598 doi:10.1175/JCLI-D-14-00152.1. [online] Available from:
 599 <http://journals.ametsoc.org/doi/abs/10.1175/JCLI-D-14-00152.1> (Accessed 3
 600 August 2014)

601 Camargo, S. J. (2013), Global and Regional Aspects of Tropical Cyclone Activity in the
 602 CMIP5 Models, *J. Clim.*, *26*(24), 9880–9902, doi:10.1175/JCLI-D-12-00549.1.

603 Camargo, S. J., and S. E. Zebiak (2002), Improving the detection and tracking of
 604 tropical cyclones in atmospheric general circulation models, *Weather Forecast.*,
 605 *17*(6), 1152–1162.

606 Camargo, S. J., A. G. Barnston, and S. E. Zebiak (2005), A statistical assessment of
 607 tropical cyclone activity in atmospheric general circulation models, *Tellus A*, *57*(4),
 608 doi:10.3402/tellusa.v57i4.14705. [online] Available from:
 609 <http://www.tellusa.net/index.php/tellusa/article/view/14705> (Accessed 3 August
 610 2014)

611 Cheng, L., J. Zhu, and R. L. Sriver (2014), Global representation of tropical cyclone-
 612 induced ocean thermal changes using Argo data – Part 1: Methods and results,
 613 *Ocean Sci Discuss*, *11*(6), 2831–2878, doi:10.5194/osd-11-2831-2014.

614 Danabasoglu, G., S. C. Bates, B. P. Briegleb, S. R. Jayne, M. Jochum, W. G. Large, S.
 615 Peacock, and S. G. Yeager (2012), The CCSM4 Ocean Component, *J. Clim.*, *25*(5),
 616 1361–1389, doi:10.1175/JCLI-D-11-00091.1.

617 Dare, R. A., and J. L. McBride (2011), Sea Surface Temperature Response to Tropical
 618 Cyclones, *Mon. Weather Rev.*, *139*(12), 3798–3808, doi:10.1175/MWR-D-10-
 619 05019.1.

620 D’Asaro, E. A., T. B. Sanford, P. P. Niiler, and E. J. Terrill (2007), Cold wake of
 621 Hurricane Frances, *Geophys. Res. Lett.*, *34*(15), L15609, doi:10.1029/2007GL030160.

622 Emanuel, K. (2001), Contribution of tropical cyclones to meridional heat transport
 623 by the oceans, *J. Geophys. Res. Atmospheres*, *106*(D14), 14771–14781,
 624 doi:10.1029/2000JD900641.

625 Gentemann, C. L. (2003), Diurnal signals in satellite sea surface temperature
 626 measurements, *Geophys. Res. Lett.*, *30*(3), doi:10.1029/2002GL016291. [online]
 627 Available from: <http://doi.wiley.com/10.1029/2002GL016291> (Accessed 8
 628 September 2014)

629 Gentemann, C. L. (2004), In situ validation of Tropical Rainfall Measuring Mission
630 microwave sea surface temperatures, *J. Geophys. Res.*, *109*(C4),
631 doi:10.1029/2003JC002092. [online] Available from:
632 <http://doi.wiley.com/10.1029/2003JC002092> (Accessed 8 September 2014)

633 Gentemann, C. L., T. Meissner, and F. J. Wentz (2010), Accuracy of Satellite Sea
634 Surface Temperatures at 7 and 11 GHz, *IEEE Trans. Geosci. Remote Sens.*, *48*(3),
635 1009–1018, doi:10.1109/TGRS.2009.2030322.

636 Gent, P. R., S. G. Yeager, R. B. Neale, S. Levis, and D. A. Bailey (2010), Improvements
637 in a half degree atmosphere/land version of the CCSM, *Clim. Dyn.*, *34*(6), 819–833,
638 doi:10.1007/s00382-009-0614-8.

639 Gualdi, S., E. Scoccimarro, and A. Navarra (2008), Changes in Tropical Cyclone
640 Activity due to Global Warming: Results from a High-Resolution Coupled General
641 Circulation Model, *J. Clim.*, *21*(20), 5204–5228, doi:10.1175/2008JCLI1921.1.

642 Haney, S., S. Bachman, B. Cooper, S. Kupper, K. McCaffrey, L. Van Roekel, S.
643 Stevenson, B. Fox-Kemper, and R. Ferrari (2012), Hurricane wake restratification
644 rates of one-, two-and three-dimensional processes, *J. Mar. Res.*, *70*(6), 824–850.

645 Hart, R. E. (2011), An inverse relationship between aggregate northern hemisphere
646 tropical cyclone activity and subsequent winter climate, *Geophys. Res. Lett.*, *38*(1),
647 L01705, doi:10.1029/2010GL045612.

648 Hart, R. E., R. N. Maue, and M. C. Watson (2007), Estimating Local Memory of
649 Tropical Cyclones through MPI Anomaly Evolution, *Mon. Weather Rev.*, *135*(12),
650 3990–4005, doi:10.1175/2007MWR2038.1.

651 Hu, A., and G. A. Meehl (2009), Effect of the Atlantic hurricanes on the oceanic
652 meridional overturning circulation and heat transport, *Geophys. Res. Lett.*, *36*(3),
653 L03702, doi:10.1029/2008GL036680.

654 Huang, P., T. B. Sanford, and J. Imberger (2009), Heat and turbulent kinetic energy
655 budgets for surface layer cooling induced by the passage of Hurricane Frances
656 (2004), *J. Geophys. Res.*, *114*(C12), doi:10.1029/2009JC005603. [online] Available
657 from: <http://doi.wiley.com/10.1029/2009JC005603> (Accessed 22 August 2014)

658 Jansen, M., and R. Ferrari (2009), Impact of the latitudinal distribution of tropical
659 cyclones on ocean heat transport, *Geophys. Res. Lett.*, *36*(6),
660 doi:10.1029/2008GL036796. [online] Available from:
661 <http://doi.wiley.com/10.1029/2008GL036796> (Accessed 20 August 2014)

662 Jansen, M. F., R. Ferrari, and T. A. Mooring (2010), Seasonal versus permanent
663 thermocline warming by tropical cyclones, *Geophys. Res. Lett.*, *37*(3), L03602,
664 doi:10.1029/2009GL041808.

665 Jullien, S., C. E. Menkes, P. Marchesiello, N. C. Jourdain, M. Lengaigne, A. Koch-
 666 Larrouy, J. Lefèvre, E. M. Vincent, and V. Faure (2012), Impact of Tropical Cyclones
 667 on the Heat Budget of the South Pacific Ocean, *J. Phys. Oceanogr.*, 42(11), 1882–1906,
 668 doi:10.1175/JPO-D-11-0133.1.

669 Jullien, S., P. Marchesiello, C. E. Menkes, J. Lefèvre, N. C. Jourdain, G. Samson, and M.
 670 Lengaigne (2014), Ocean feedback to tropical cyclones: climatology and processes,
 671 *Clim. Dyn.*, 1–24, doi:10.1007/s00382-014-2096-6.

672 Kim, H.-S., G. A. Vecchi, T. R. Knutson, W. G. Anderson, T. L. Delworth, A. Rosati, F.
 673 Zeng, and M. Zhao (2014), Tropical Cyclone Simulation and Response to CO2
 674 Doubling in the GFDL CM2.5 High-Resolution Coupled Climate Model, *J. Clim.*,
 675 doi:10.1175/JCLI-D-13-00475.1. [online] Available from:
 676 <http://journals.ametsoc.org/doi/abs/10.1175/JCLI-D-13-00475.1> (Accessed 2
 677 September 2014)

678 Kirtman, B. P. et al. (2012), Impact of ocean model resolution on CCSM climate
 679 simulations, *Clim. Dyn.*, 39(6), 1303–1328, doi:10.1007/s00382-012-1500-3.

680 Le Traon, P. Y., F. Nadal, and N. Ducet (1998), An improved mapping method of
 681 multisatellite altimeter data, *J. Atmospheric Ocean. Technol.*, 15(2), 522–534.

682 Li, F., W. D. Collins, M. F. Wehner, and L. R. Leung (2013), Hurricanes in an
 683 aquaplanet world: Implications of the impacts of external forcing and model
 684 horizontal resolution: IMPACT OF MODEL RESOLUTION ON HURRICANES, *J. Adv.*
 685 *Model. Earth Syst.*, 5(2), 134–145, doi:10.1002/jame.20020.

686 Liu, J., J. A. Curry, C. A. Clayson, and M. A. Bourassa (2011), High-Resolution Satellite
 687 Surface Latent Heat Fluxes in North Atlantic Hurricanes, *Mon. Weather Rev.*, 139(9),
 688 2735–2747, doi:10.1175/2011MWR3548.1.

689 Lloyd, I. D., and G. A. Vecchi (2011), Observational Evidence for Oceanic Controls on
 690 Hurricane Intensity, *J. Clim.*, 24(4), 1138–1153, doi:10.1175/2010JCLI3763.1.

691 Maltrud, M. E., and J. L. McClean (2005), An eddy resolving global 1/10° ocean
 692 simulation, *Ocean Model.*, 8(1-2), 31–54, doi:10.1016/j.ocemod.2003.12.001.

693 Manganello, J. V. et al. (2012), Tropical Cyclone Climatology in a 10-km Global
 694 Atmospheric GCM: Toward Weather-Resolving Climate Modeling, *J. Clim.*, 25(11),
 695 3867–3893, doi:10.1175/JCLI-D-11-00346.1.

696 McClean, J. L., P.-M. Poulain, J. W. Pelton, and M. E. Maltrud (2002), Eulerian and
 697 Lagrangian Statistics from Surface Drifters and a High-Resolution POP Simulation in
 698 the North Atlantic, *J. Phys. Oceanogr.*, 32(9), 2472–2491, doi:10.1175/1520-0485-
 699 32.9.2472.

700 McClean, J. L. et al. (2011), A prototype two-decade fully-coupled fine-resolution
 701 CCSM simulation, *Ocean Model.*, 39(1–2), 10–30, doi:10.1016/j.ocemod.2011.02.011.

702 Mei, W., and C. Pasquero (2012), Spatial and Temporal Characterization of Sea
 703 Surface Temperature Response to Tropical Cyclones*, *J. Clim.*, 26(11), 3745–3765,
 704 doi:10.1175/JCLI-D-12-00125.1.

705 Mei, W., F. Primeau, J. C. McWilliams, and C. Pasquero (2013), Sea surface height
 706 evidence for long-term warming effects of tropical cyclones on the ocean, *Proc. Natl.*
 707 *Acad. Sci.*, 201306753, doi:10.1073/pnas.1306753110.

708 Murakami, H., and M. Sugi (2010), Effect of Model Resolution on Tropical Cyclone
 709 Climate Projections, *Sola*, 6, 73–76, doi:10.2151/sola.2010-019.

710 Neale, R. B., J. H. Richter, and M. Jochum (2008), The Impact of Convection on ENSO:
 711 From a Delayed Oscillator to a Series of Events, *J. Clim.*, 21(22), 5904–5924,
 712 doi:10.1175/2008JCLI2244.1.

713 Park, J. J., Y.-O. Kwon, and J. F. Price (2011), Argo array observation of ocean heat
 714 content changes induced by tropical cyclones in the north Pacific, *J. Geophys. Res.*
 715 *Oceans*, 116(C12), C12025, doi:10.1029/2011JC007165.

716 Pasquero, C., and K. Emanuel (2008), Tropical Cyclones and Transient Upper-Ocean
 717 Warming, *J. Clim.*, 21(1), 149–162, doi:10.1175/2007JCLI1550.1.

718 Rathmann, N. M., S. Yang, and E. Kaas (2014), Tropical cyclones in enhanced
 719 resolution CMIP5 experiments, *Clim. Dyn.*, 42(3–4), 665–681, doi:10.1007/s00382-
 720 013-1818-5.

721 Scoccimarro, E., S. Gualdi, A. Bellucci, A. Sanna, P. Giuseppe Fogli, E. Manzini, M.
 722 Vichi, P. Oddo, and A. Navarra (2011), Effects of Tropical Cyclones on Ocean Heat
 723 Transport in a High-Resolution Coupled General Circulation Model, *J. Clim.*, 24(16),
 724 4368–4384, doi:10.1175/2011JCLI4104.1.

725 Shaevitz, D. A. et al. (n.d.), Characteristics of tropical cyclones in high-resolution,
 726 [online] Available from:
 727 http://www.ldeo.columbia.edu/~sobel/Papers/shaevitz_etal_HWG.pdf (Accessed 3
 728 September 2014)

729 Small, R. J. et al. (2014), A new synoptic scale resolving global climate simulation
 730 using the Community Earth System Model, *J. Adv. Model. Earth Syst.*, 6(4), 1065–
 731 1094, doi:10.1002/2014MS000363.

732 Smith, R. D., M. E. Maltrud, F. O. Bryan, and M. W. Hecht (2000), Numerical
 733 Simulation of the North Atlantic Ocean at 1/10°, *J. Phys. Oceanogr.*, 30(7), 1532–
 734 1561, doi:10.1175/1520-0485(2000)030<1532:NSOTNA>2.0.CO;2.

735 Sriver, R. L. (2013), Observational evidence supports the role of tropical cyclones in
736 regulating climate, *Proc. Natl. Acad. Sci.*, *110*(38), 15173–15174,
737 doi:10.1073/pnas.1314721110.

738 Sriver, R. L., and M. Huber (2007), Observational evidence for an ocean heat pump
739 induced by tropical cyclones, *Nature*, *447*(7144), 577–580,
740 doi:10.1038/nature05785.

741 Sriver, R. L., and M. Huber (2010), Modeled sensitivity of upper thermocline
742 properties to tropical cyclone winds and possible feedbacks on the Hadley
743 circulation: CCSM SENSITIVITY TO TC WINDS, *Geophys. Res. Lett.*, *37*(8), n/a–n/a,
744 doi:10.1029/2010GL042836.

745 Sriver, R. L., M. Huber, and J. Nusbaumer (2008), Investigating tropical cyclone-
746 climate feedbacks using the TRMM Microwave Imager and the Quick Scatterometer,
747 *Geochem. Geophys. Geosystems*, *9*(9), Q09V11, doi:10.1029/2007GC001842.

748 Sriver, R. L., M. Goes, M. E. Mann, and K. Keller (2010), Climate response to tropical
749 cyclone-induced ocean mixing in an Earth system model of intermediate complexity,
750 *J. Geophys. Res. Oceans*, *115*(C10), C10042, doi:10.1029/2010JC006106.

751 Strachan, J., P. L. Vidale, K. Hodges, M. Roberts, and M.-E. Demory (2012),
752 Investigating Global Tropical Cyclone Activity with a Hierarchy of AGCMs: The Role
753 of Model Resolution, *J. Clim.*, *26*(1), 133–152, doi:10.1175/JCLI-D-12-00012.1.

754 Vincent, E. M., G. Madec, M. Lengaigne, J. Vialard, and A. Koch-Larrouy (2013),
755 Influence of tropical cyclones on sea surface temperature seasonal cycle and ocean
756 heat transport, *Clim. Dyn.*, *41*(7-8), 2019–2038, doi:10.1007/s00382-012-1556-0.

757 Walsh, K., S. Lavender, E. Scoccimarro, and H. Murakami (2013), Resolution
758 dependence of tropical cyclone formation in CMIP3 and finer resolution models,
759 *Clim. Dyn.*, *40*(3-4), 585–599, doi:10.1007/s00382-012-1298-z.

760 Walsh, K. J. E., M. Fiorino, C. W. Landsea, and K. L. McInnes (2007), Objectively
761 Determined Resolution-Dependent Threshold Criteria for the Detection of Tropical
762 Cyclones in Climate Models and Reanalyses, *J. Clim.*, *20*(10), 2307–2314,
763 doi:10.1175/JCLI4074.1.

764 Wang, X., C. Wang, G. Han, W. Li, and X. Wu (2014), Effects of tropical cyclones on
765 large-scale circulation and ocean heat transport in the South China Sea, *Clim. Dyn.*,
766 *1–16*, doi:10.1007/s00382-014-2109-5.

767 Wehner, M. F., G. Bala, P. Duffy, A. A. Mirin, and R. Romano (2010), Towards Direct
768 Simulation of Future Tropical Cyclone Statistics in a High-Resolution Global
769 Atmospheric Model, *Adv. Meteorol.*, *2010*, e915303, doi:10.1155/2010/915303.

770 Wehner, M. F. et al. (2014), The effect of horizontal resolution on simulation quality
771 in the Community Atmospheric Model, CAM5.1, *J. Adv. Model. Earth Syst.*, 6(4), 980–
772 997, doi:10.1002/2013MS000276.

773 Zhao, M., I. M. Held, S.-J. Lin, and G. A. Vecchi (2009), Simulations of Global Hurricane
774 Climatology, Interannual Variability, and Response to Global Warming Using a 50-
775 km Resolution GCM, *J. Clim.*, 22(24), 6653–6678, doi:10.1175/2009JCLI3049.1.

776

Figures

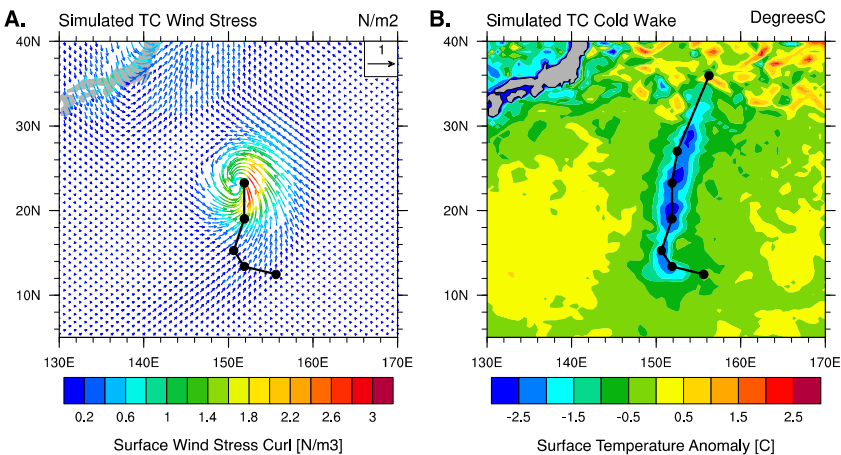
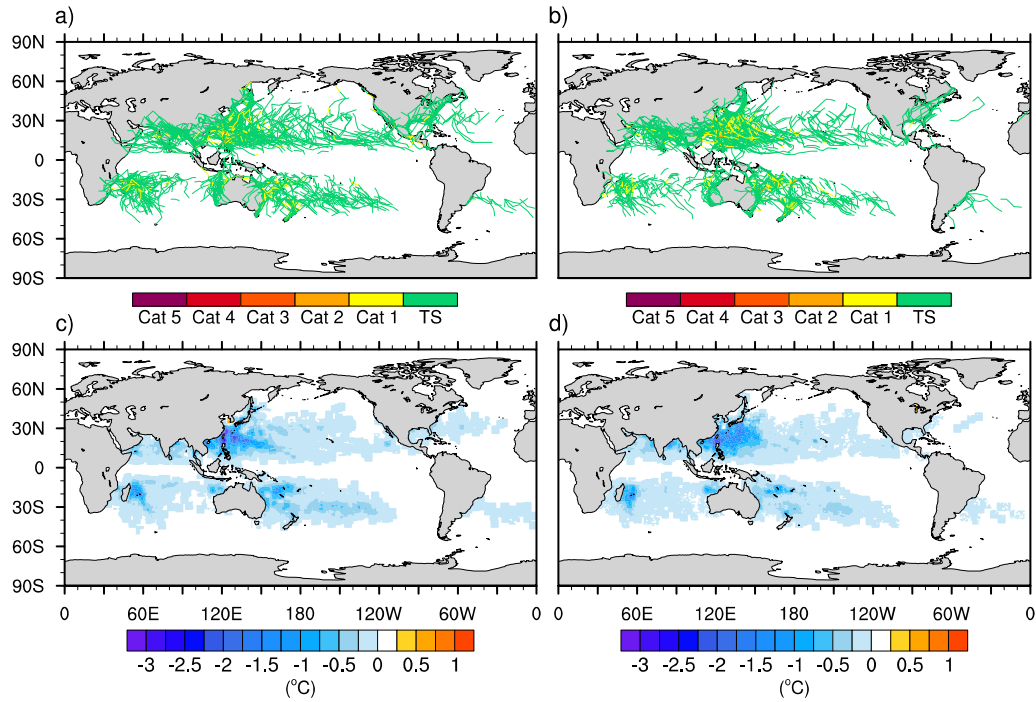


Figure 1. . A. Simulated TC circulation using CCSM3.5 with a 0.5° atmosphere model.
B. The corresponding surface temperature anomaly from the 0.1° eddy-resolving ocean component. The temperature anomaly is estimated as the post-storm minus pre-storm temperature fields.



785

786 Figure 2. Model-simulated storm tracks accumulated over 20 years in the (a) low
 787 resolution and (b) high resolution configurations. Modeled annually accumulated, storm-
 788 induced average sea surface cooling for the (c) low resolution and (d) high resolution
 789 configurations.

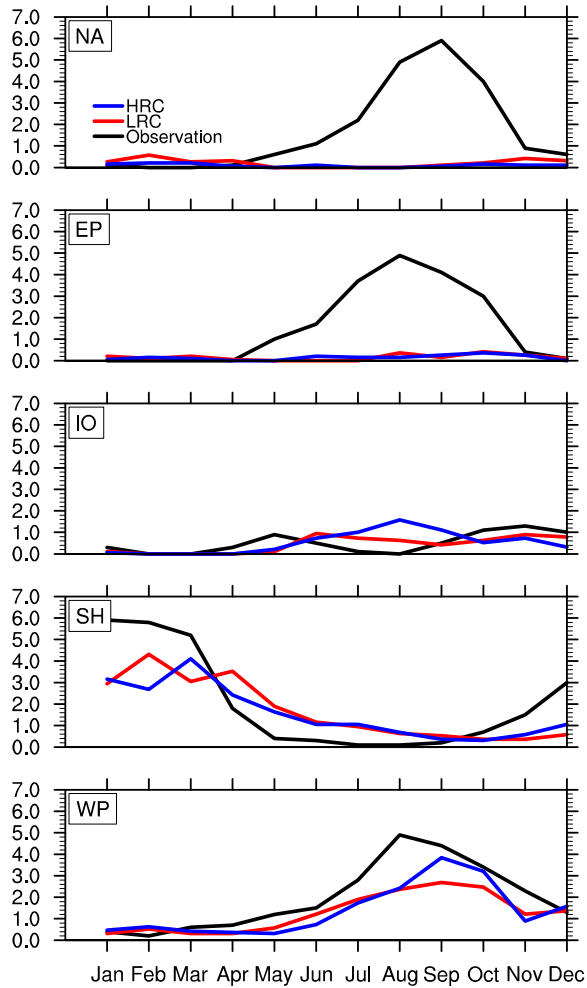
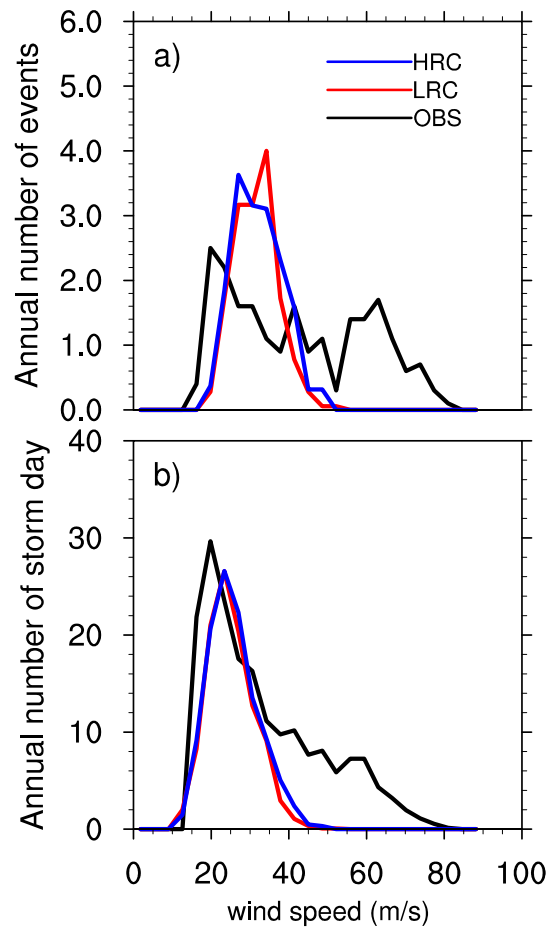


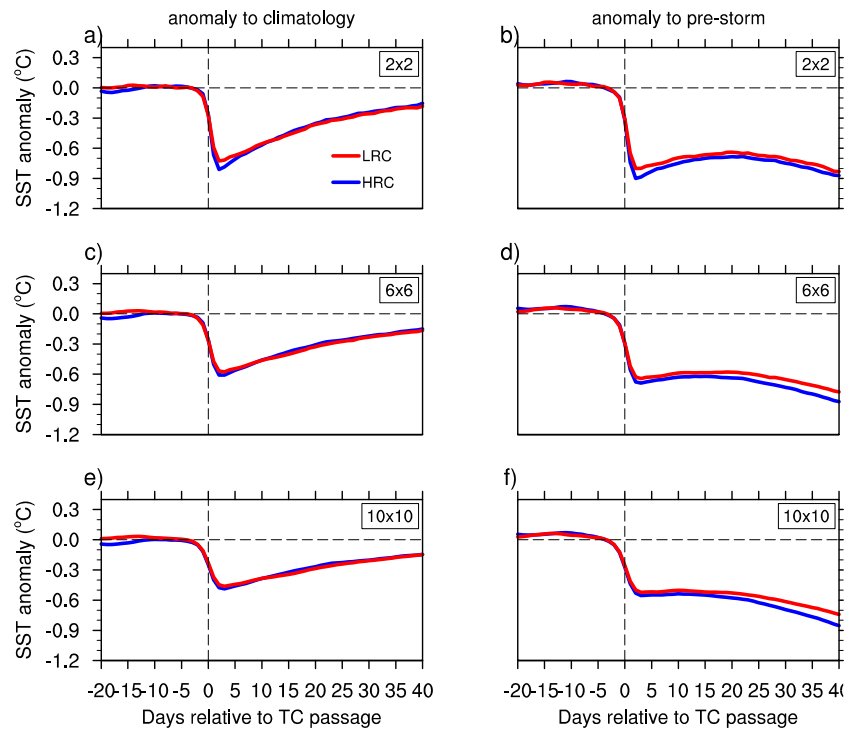
Figure 3. Monthly averaged storm counts of TCs in five tropical cyclone basins – (upper to lower) North Atlantic, East Pacific, Indian Ocean, South Hemisphere, and Northwest Pacific. Red and blue curves represent results from the low and high resolution model simulations, respectively. Black curves indicate observation-based results only considering TC up to category 3 to enable direct comparison with model results.



797

798 Figure 4. Frequency distributions of (a) the maximum wind speed of each tropical
 799 cyclone event and (b) the wind speed of each storm day in the Northwestern Pacific basin
 800 for observations (OBS), low resolution configuration (LRC) and high resolution
 801 configuration (HRC). Here we only consider storm days with wind speed exceeding 15

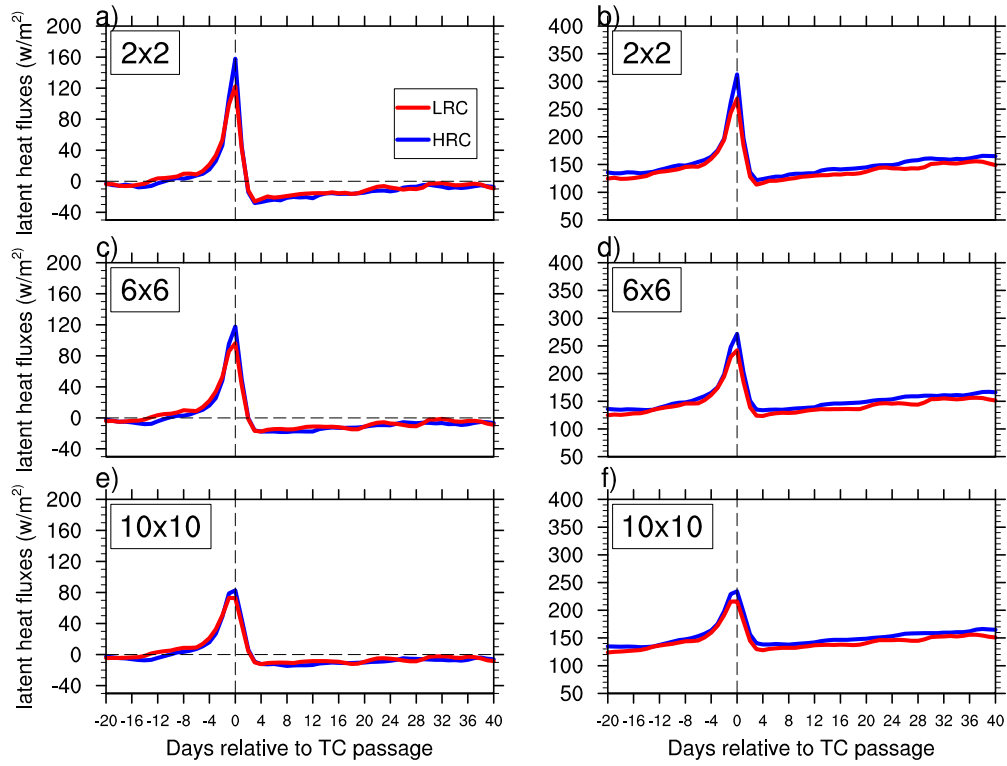
802 $m \cdot s^{-1}$.



803

804

805 Figure 5. Temporal evolution of composite TC-induced sea surface temperature
 806 anomalies relative to daily climatology (a,c,e) and anomalies relative to pre-storm
 807 conditions (b,d,f) in the Northwest Pacific basin for low-resolution simulation (LRC) and
 808 high-resolution simulation (HRC), The SST anomaly is averaged over a (top) $2^\circ \times 2^\circ$,
 809 (middle) $6^\circ \times 6^\circ$, and (bottom) $10^\circ \times 10^\circ$ TC footprint domain size that moves with the
 810 storms.

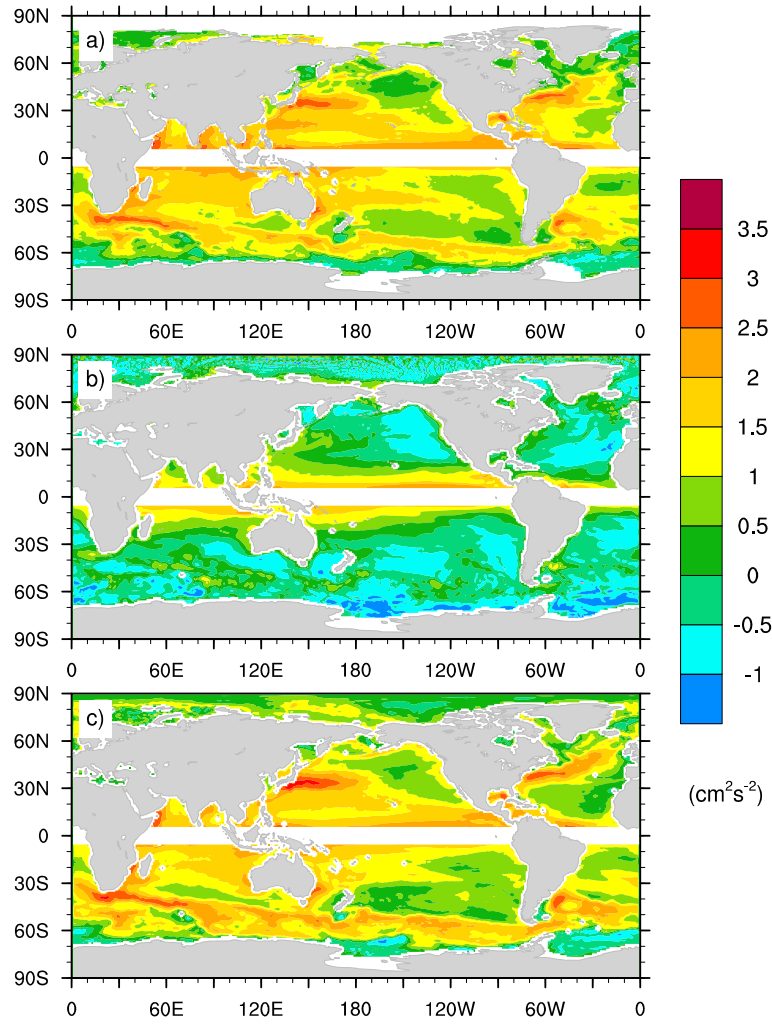


811

812 Figure 6. Temporal evolution of composite TC-induced surface latent heat fluxes
 813 anomalies relative to daily climatology (a,c,e), and their total values (b,d,f) in the
 814 Northwest Pacific basin for low-resolution simulation (LRC) and high-resolution
 815 simulation (HRC). The latent heat flux anomaly is averaged over a (top) $2^{\circ} \times 2^{\circ}$, (middle)
 816 $6^{\circ} \times 6^{\circ}$, and (bottom) $10^{\circ} \times 10^{\circ}$ footprint domain size that moves with the storms.

817

818

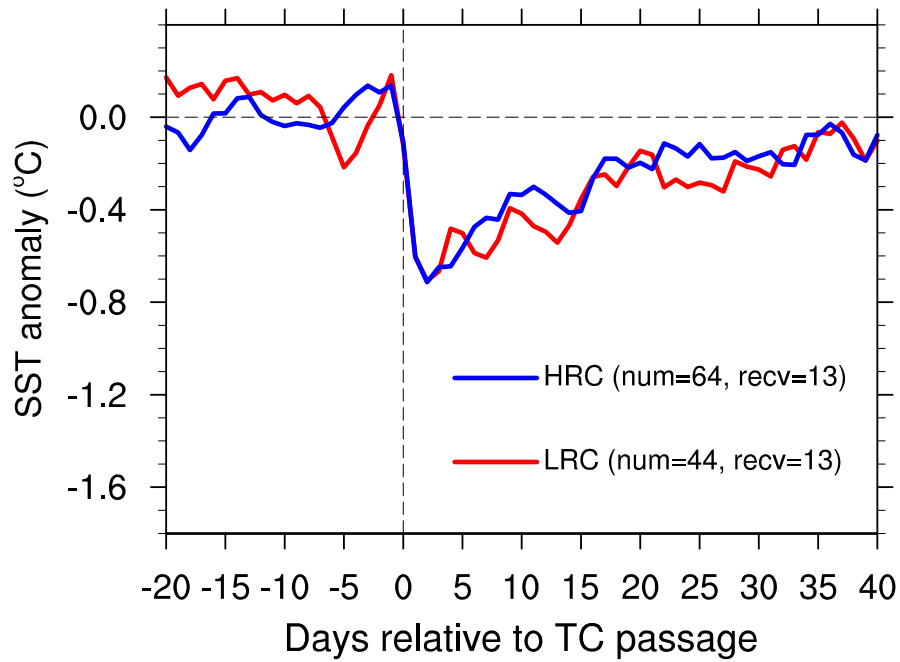


819

820 Figure 7. Logarithm of the annually averaged eddy kinetic energy (EKE) of (a) satellite-

821 based observations, (b) low-resolution model simulation, and (c) high-resolution model

822 simulation.



823

824 Figur naly

825 relative to daily climatology in the high EKE region (30° - 40° N, 130° - 175°) for high

826 resolution configuration (HRC) and low resolution configuration (LRC). The number of

827 storm days and the average e-folding time scales are denoted in the parentheses.

828

829

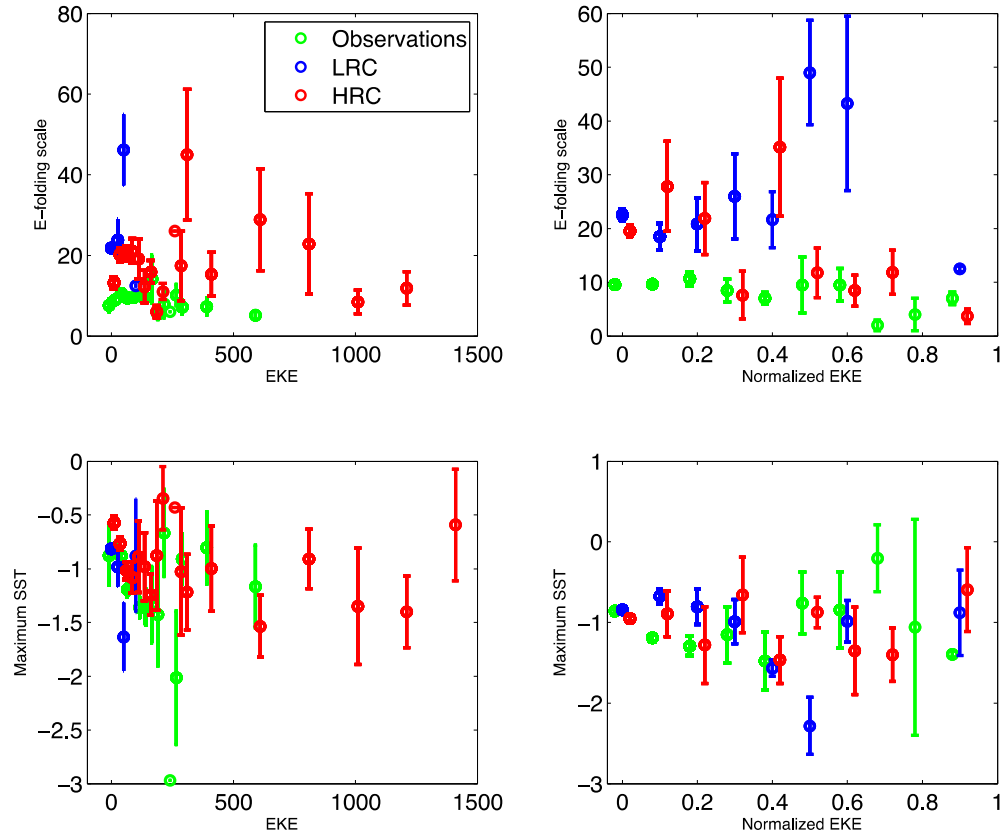
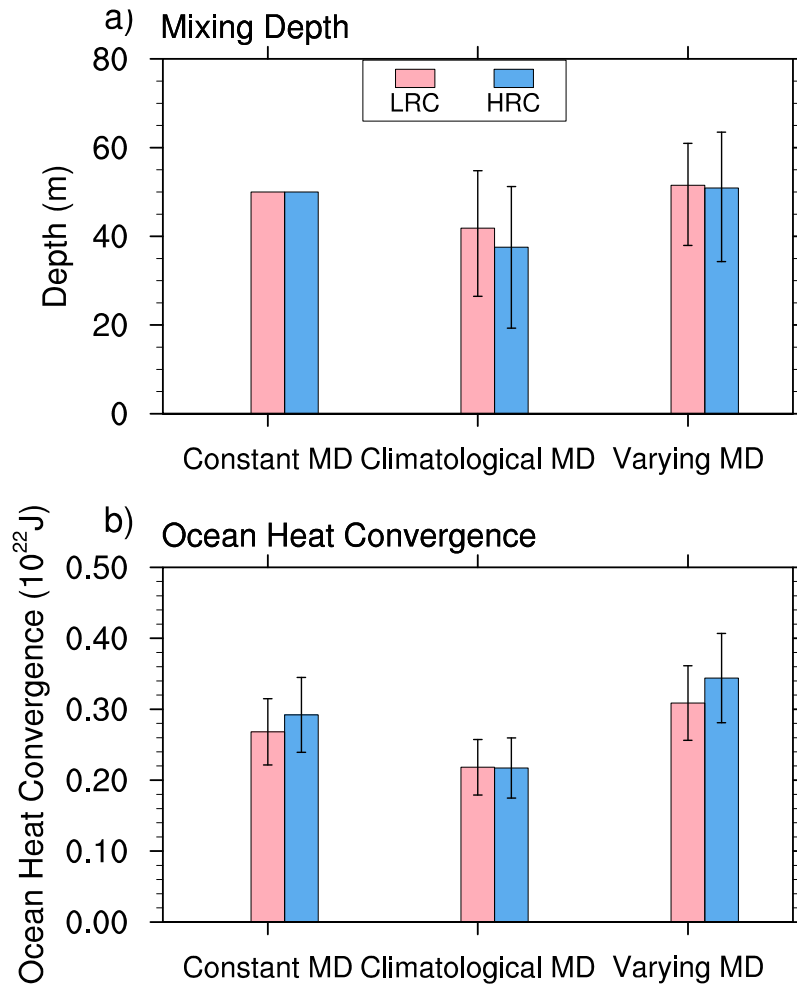


Figure 9. Relationship between EKE and e-folding time (upper panels), and between EKE and maximum sea surface cooling (lower panels) in observations (green), low resolution simulation (blue), and high resolution simulation (red). The circles are bin averages and the error bars are their respective standard errors. EKE is normalized on the right panels.



837

838 Figure 10. Composite area-mean mixing depth of each storm day in the Northwest
839 Pacific basin for low-resolution simulation (LRC) and high-resolution simulation
840 (HRC), computed with three strategies – (from left to right) constant mixing depth
841 of 50m, monthly mean climatological mixed layer depth, and varying mixing depth
842 derived from ocean potential temperature profiles. The averaging area is a $6^{\circ} \times 6^{\circ}$
843 grid box. The error bars indicate the range of mixing depth within the averaging
844 area for the analysis period (20 years). (b) Annually accumulated, storm-induced

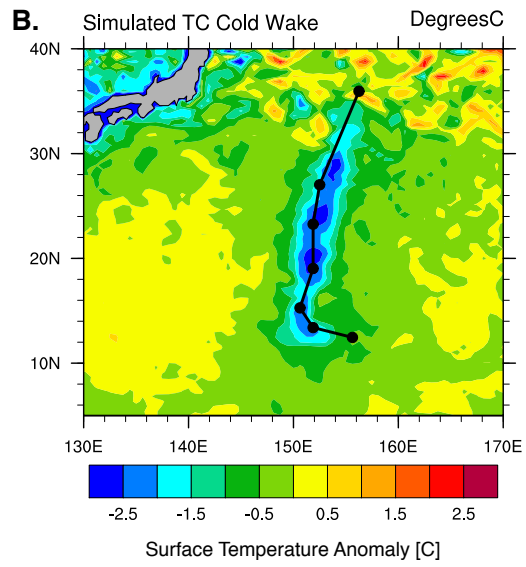
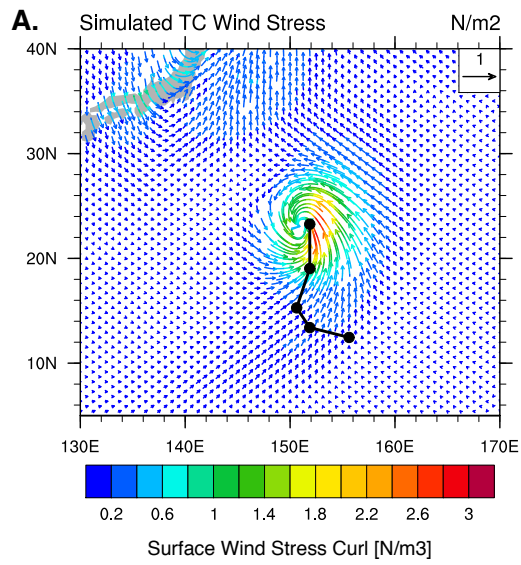
average ocean heat uptake in the Northwest Pacific basin, computed with the three corresponding mixing depth strategies. A discrete method is used to account for the non-uniform mixing within the 6°x6° averaging domain. Error bars represent the plus or minus 1 standard deviation

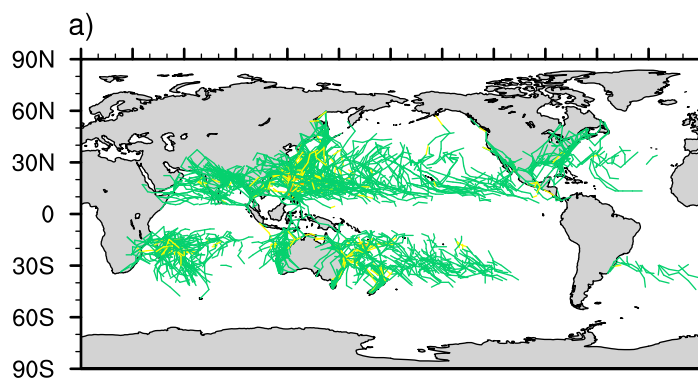
Number	OBS	LRC	HRC
Annual global storm number	92	45.7	45.3
Annual storm number in northwestern Pacific (total)	26.5	15.4	16.6

Table 1. Modeled and observation-based annual storm number.

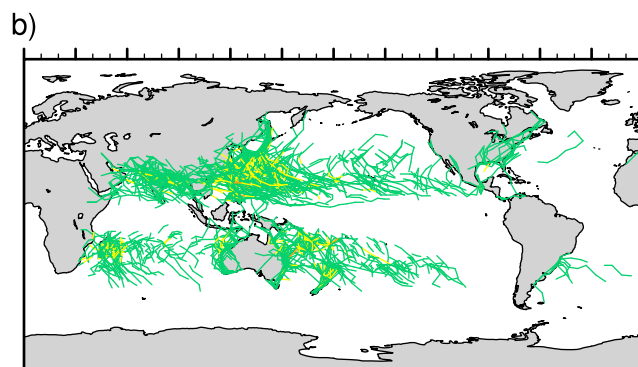
Data	LRC	HRC
Latent heat exchange (J)	1.43e+21	1.70e+21
Total OHC (J)	3.08e+21	3.57e+21
Percentage of latent heat flux in total OHC	45%	47%
Mixing-induced OHC (J)	1.65e+21	1.87e+21
Mixing-induced OHC (PW)	0.05	0.06
Standard deviation of the distribution of annual OHC	0.02143	0.03351

Table 2. Surface latent heat flux, total OHC, mixing-induced OHC, and the range and standard deviation of OHC in the two model simulations

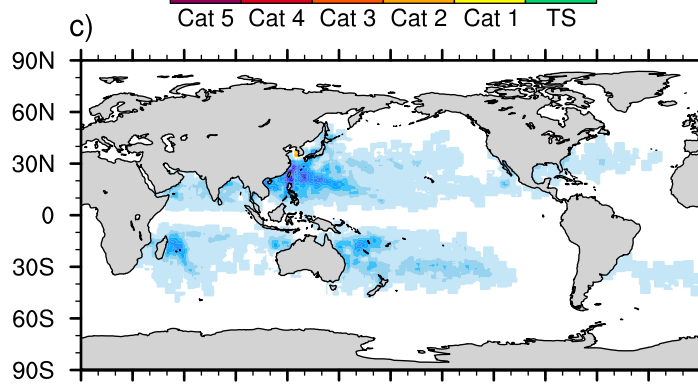




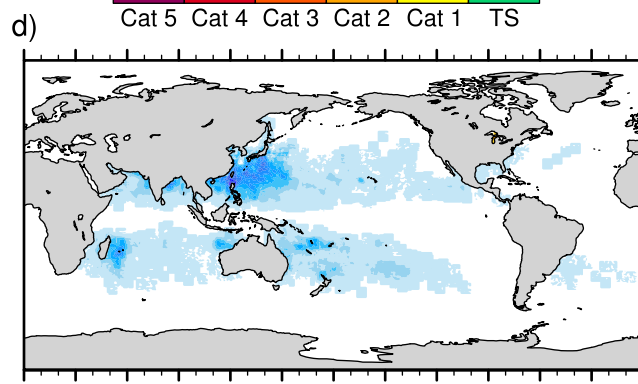
Cat 5 Cat 4 Cat 3 Cat 2 Cat 1 TS



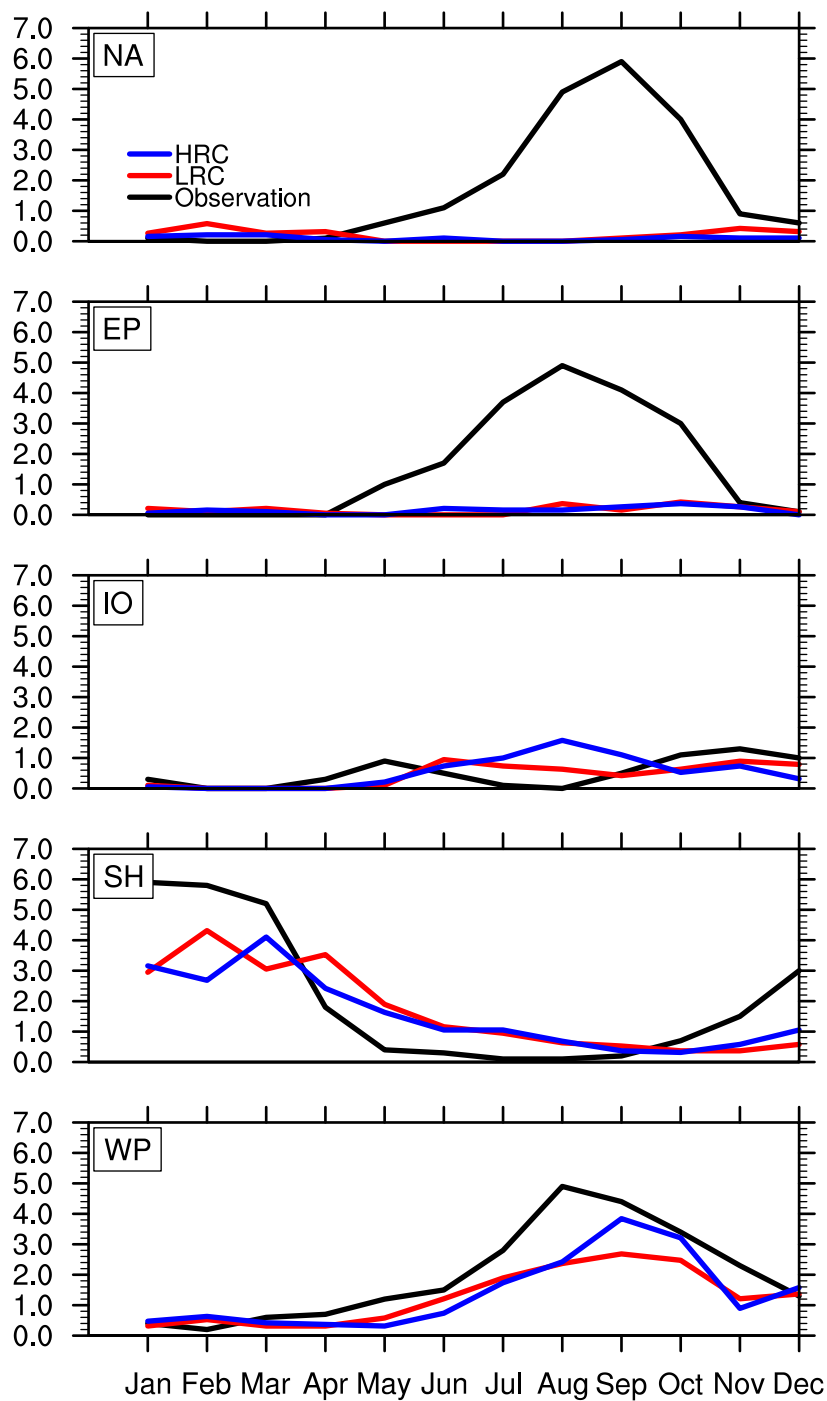
Cat 5 Cat 4 Cat 3 Cat 2 Cat 1 TS

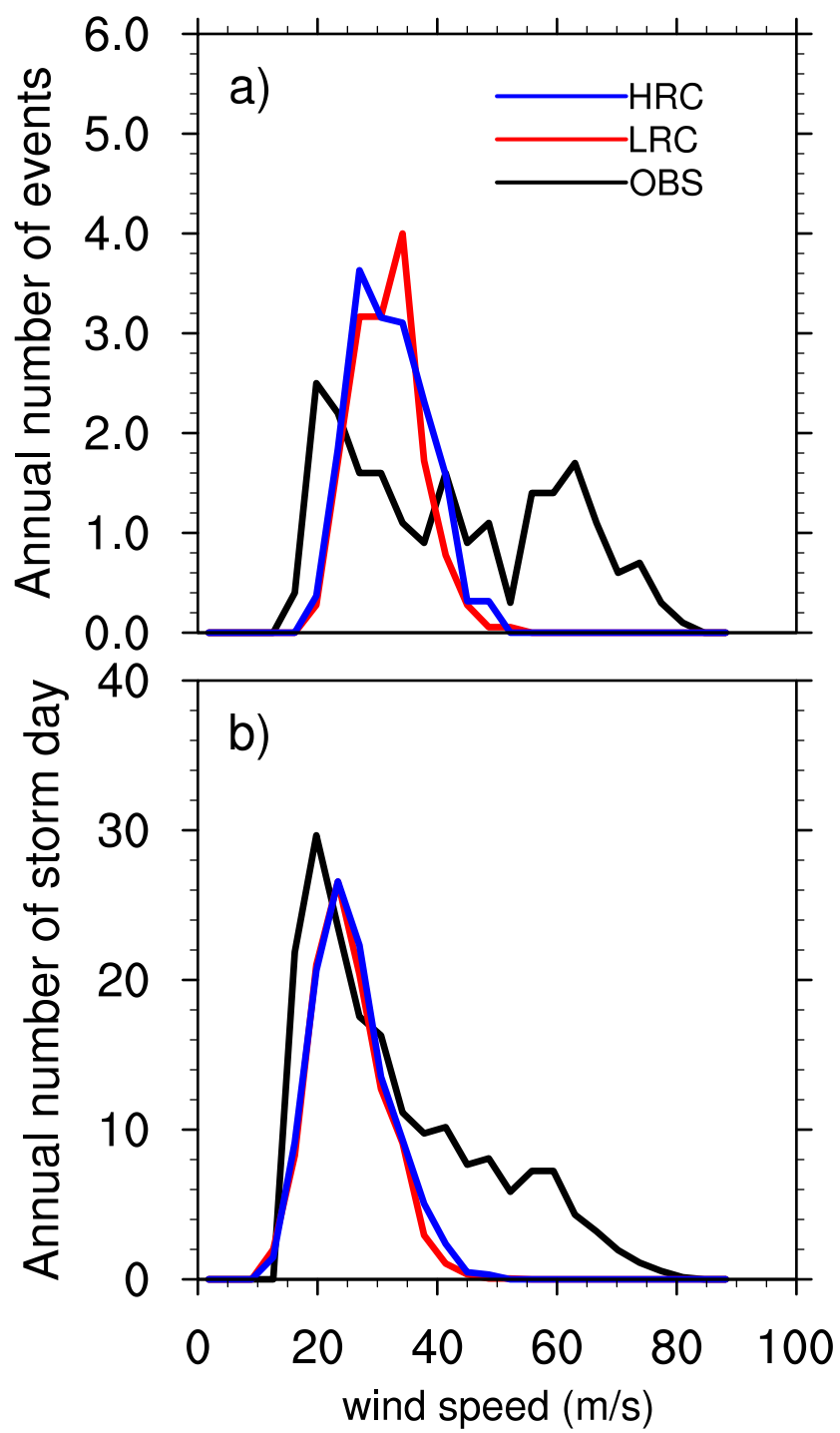


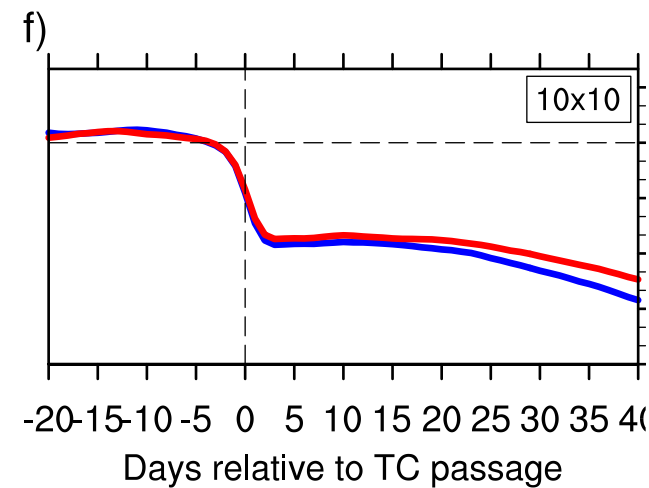
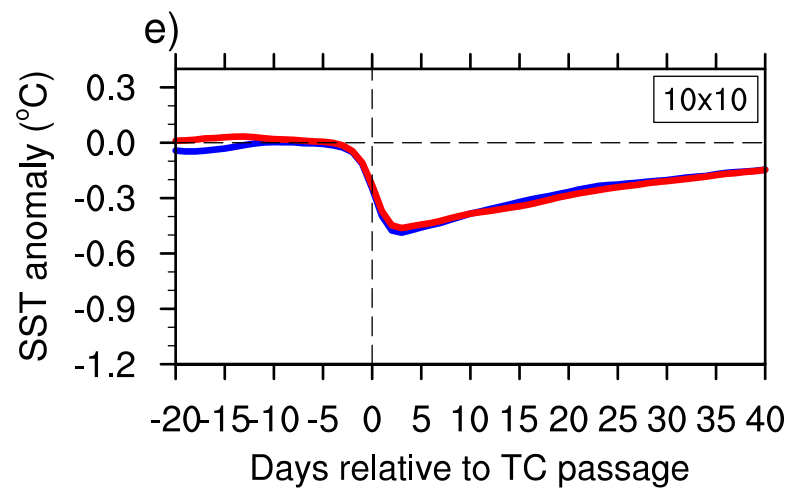
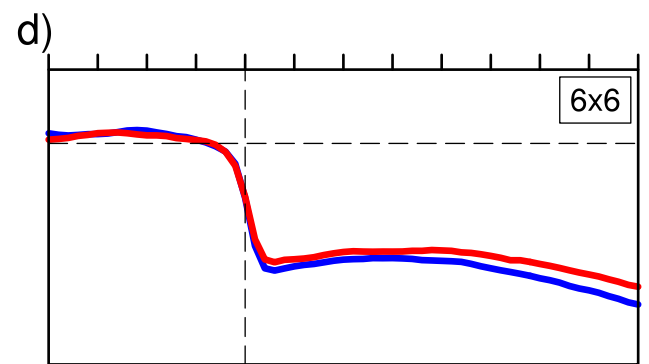
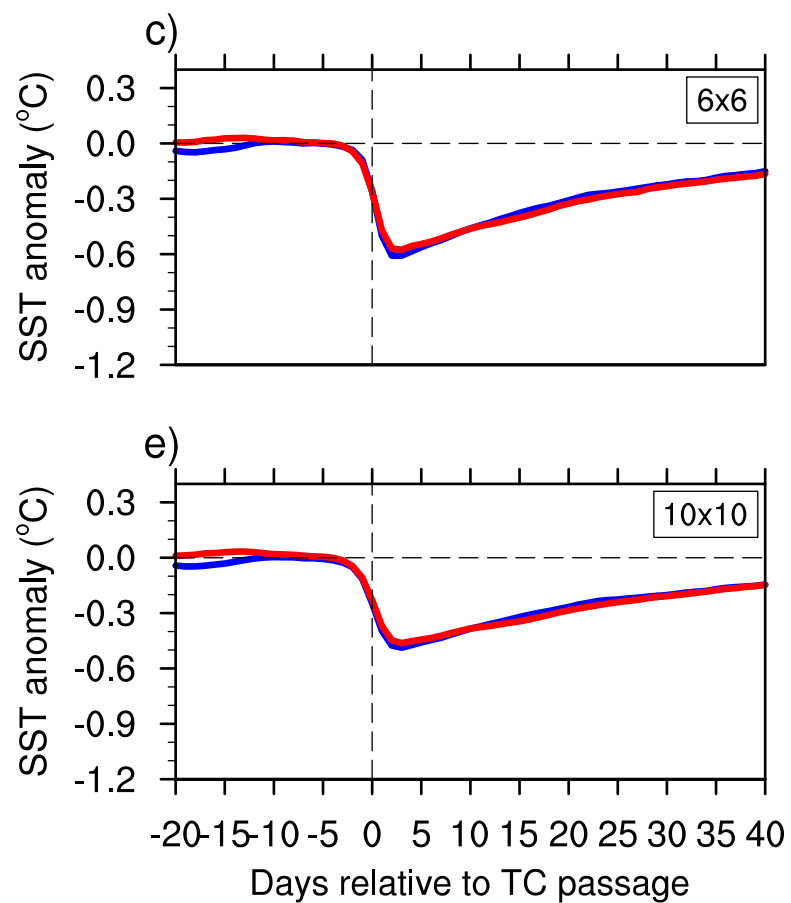
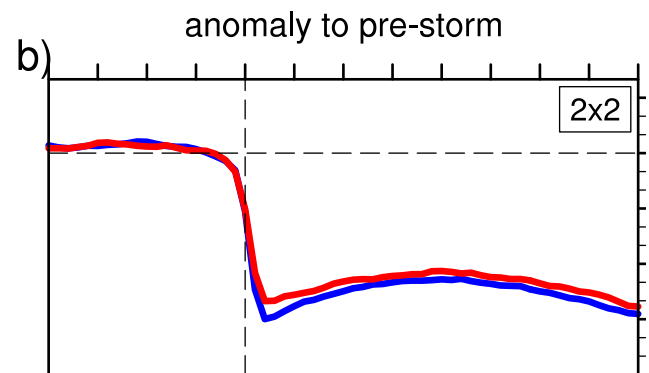
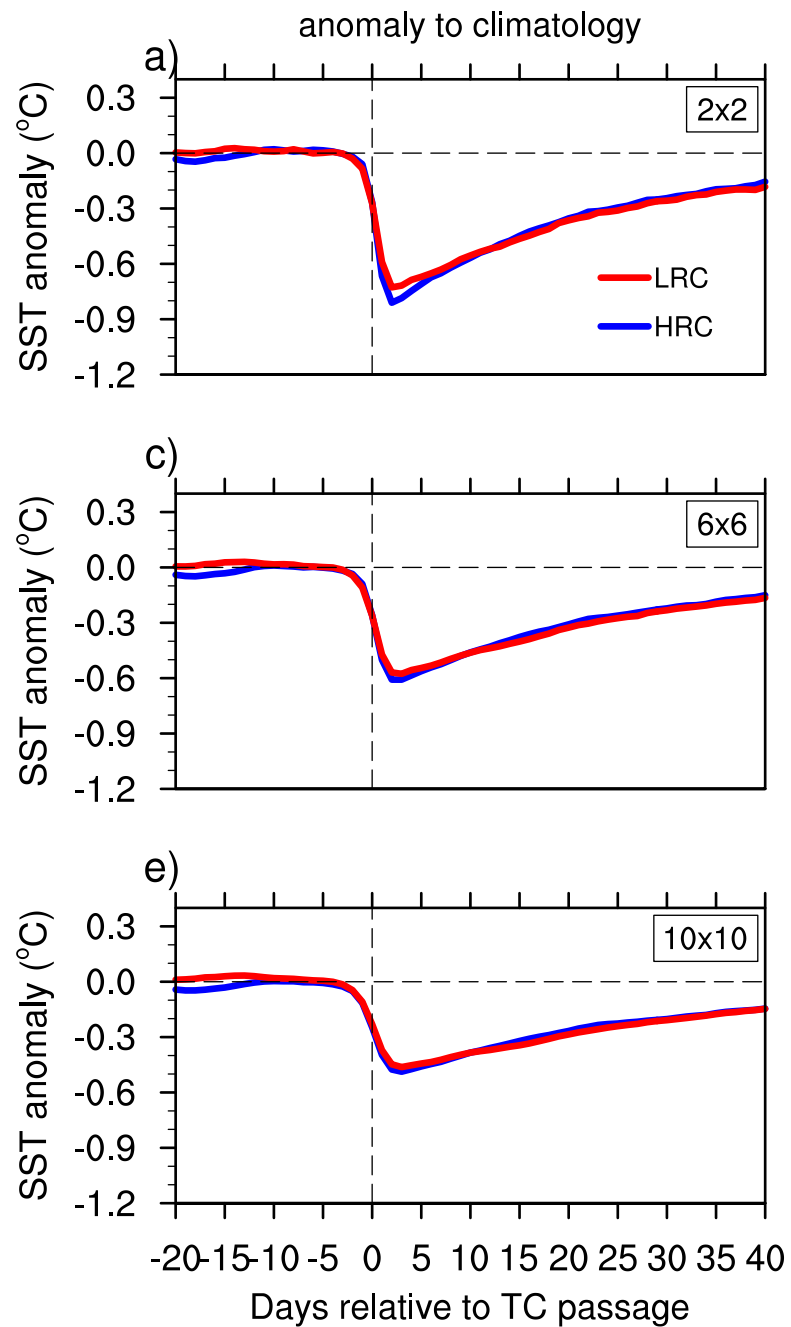
0 60E 120E 180 120W 60W
-3 -2.5 -2 -1.5 -1 -0.5 0 0.5 1
(°C)

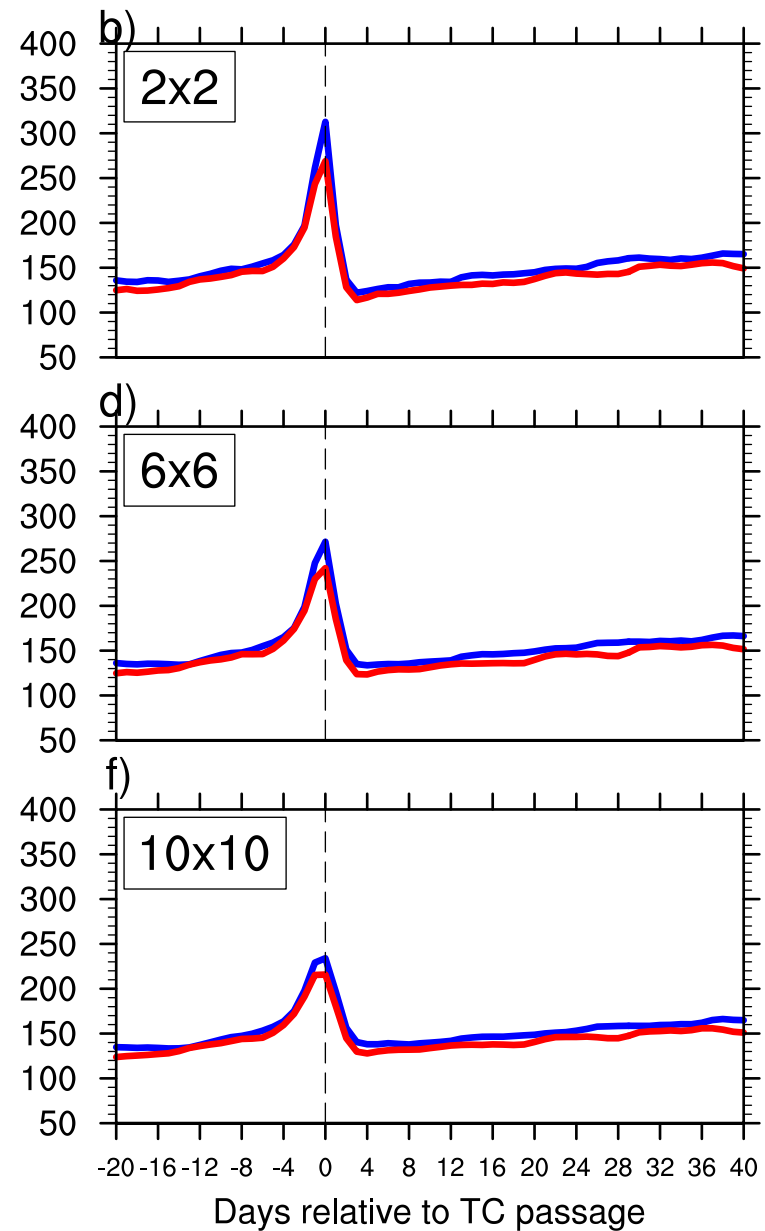
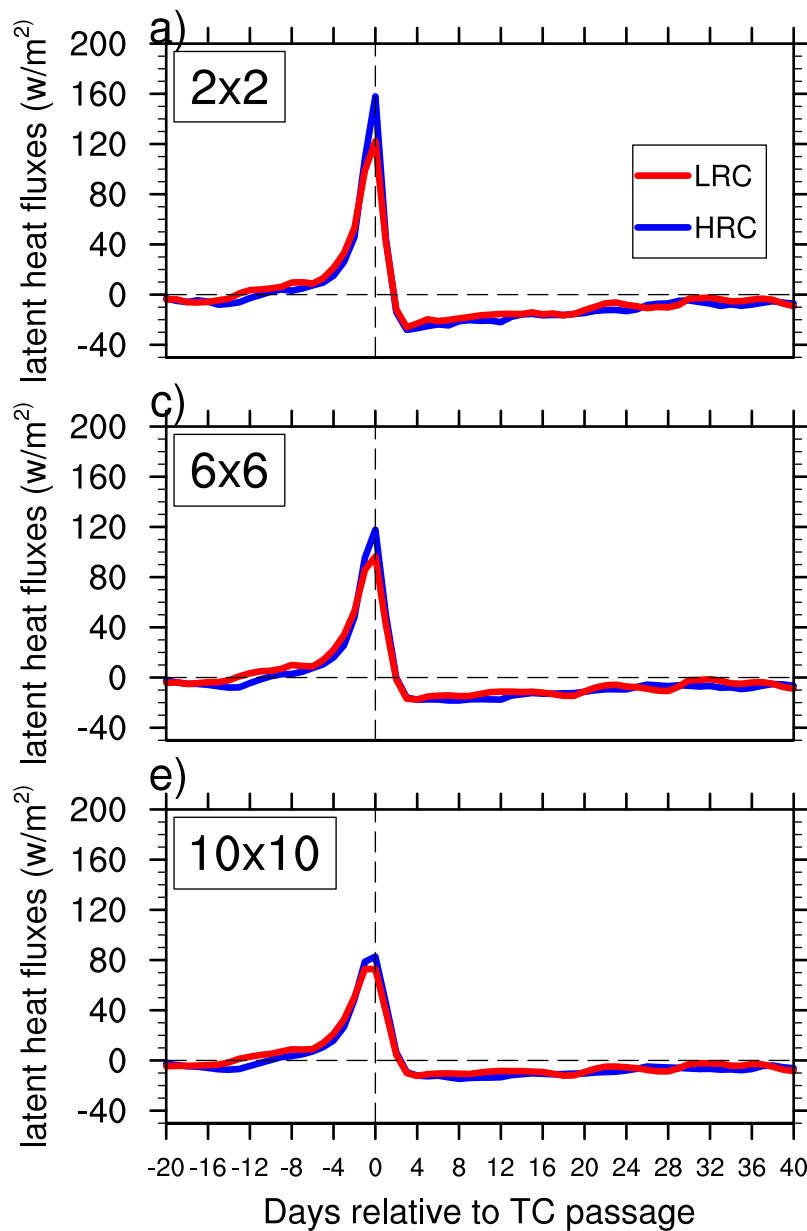


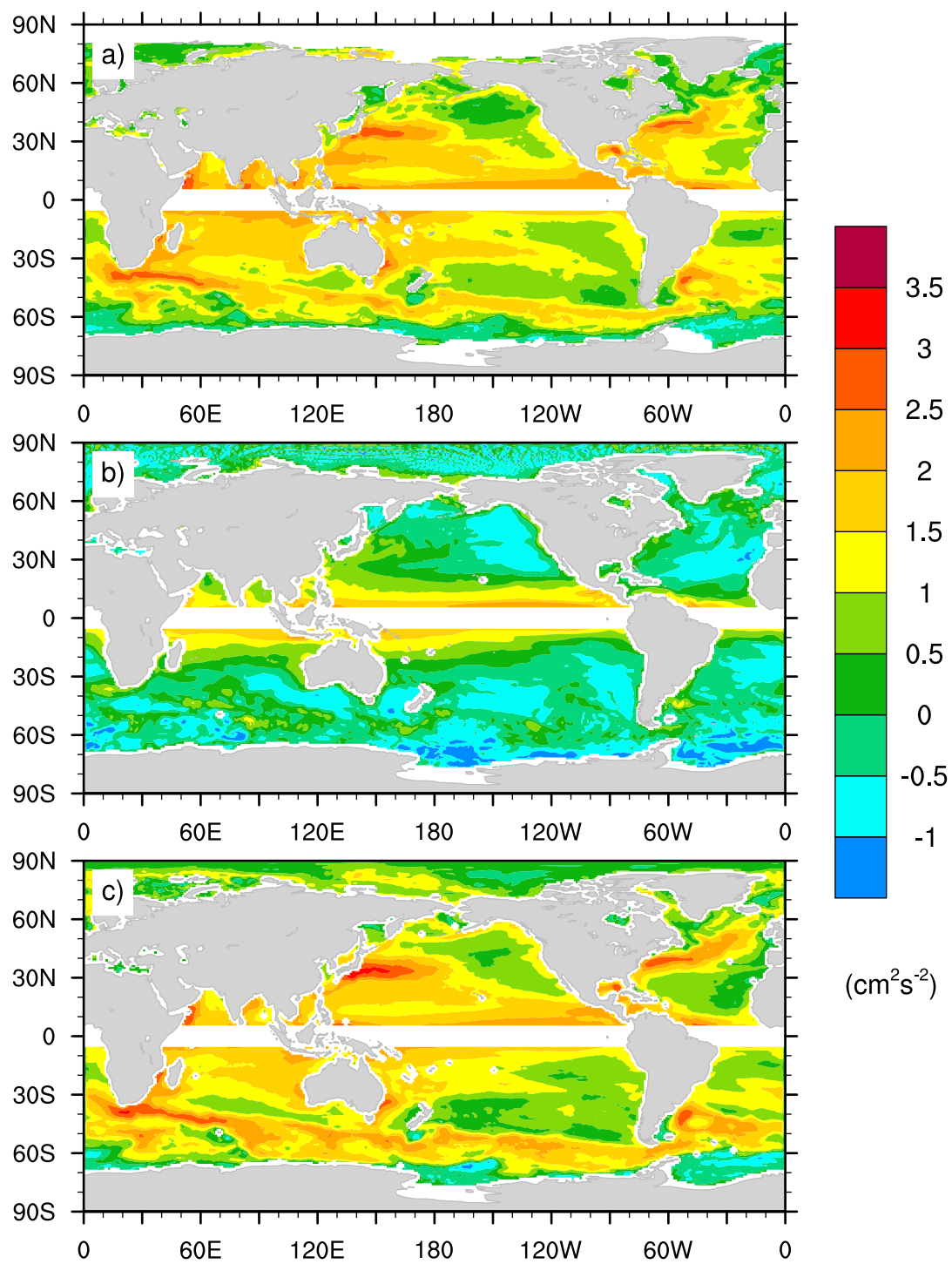
0 60E 120E 180 120W 60W 0
-3 -2.5 -2 -1.5 -1 -0.5 0 0.5 1
(°C)

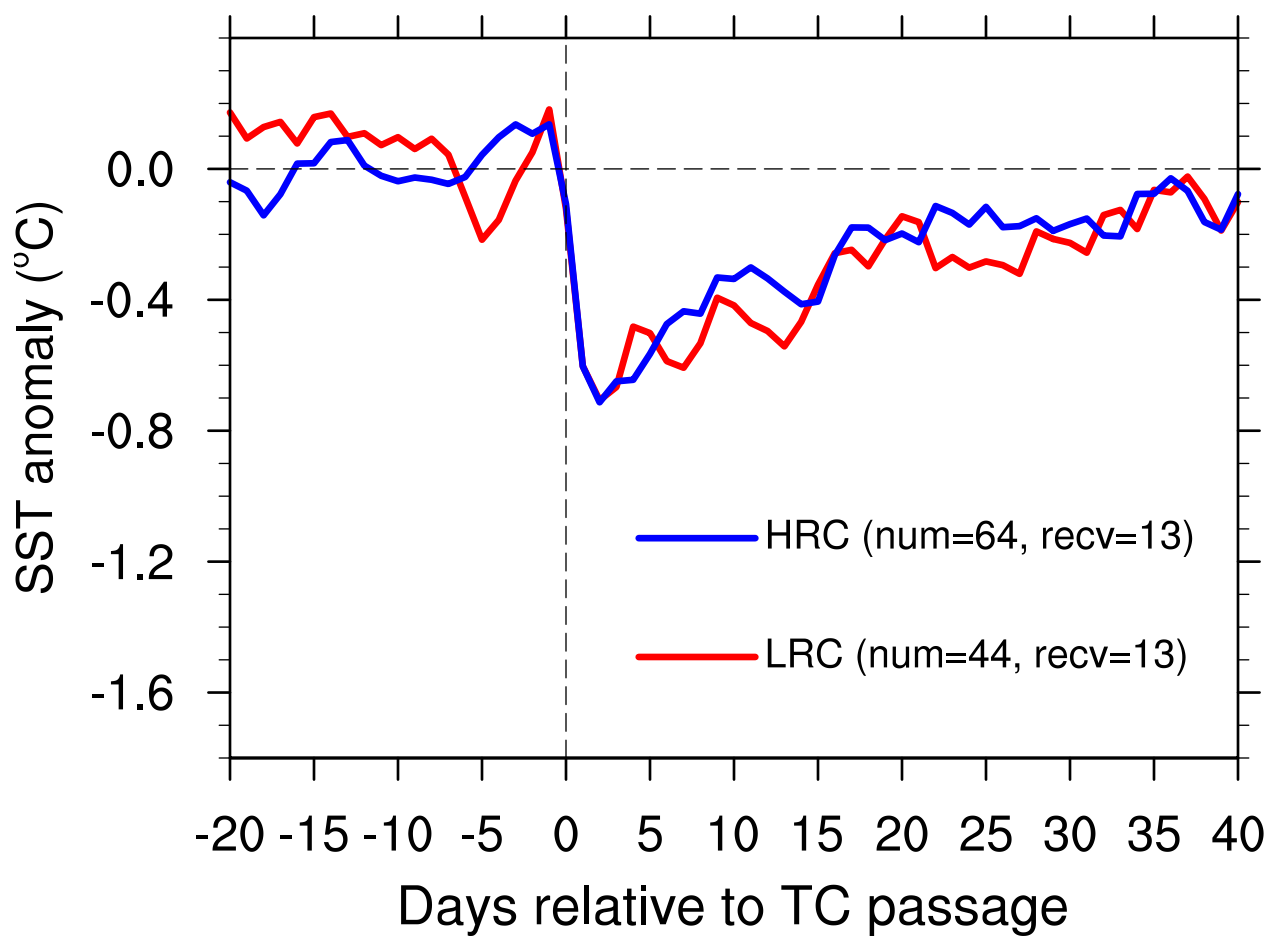


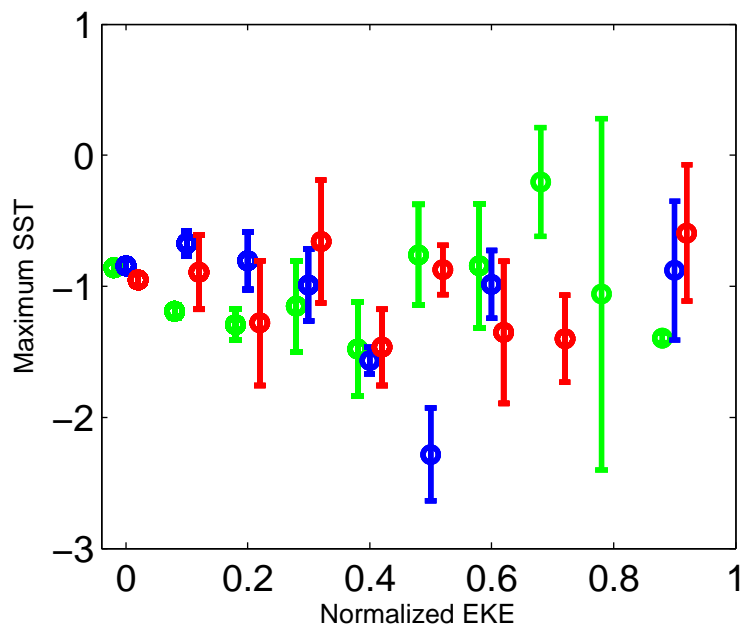
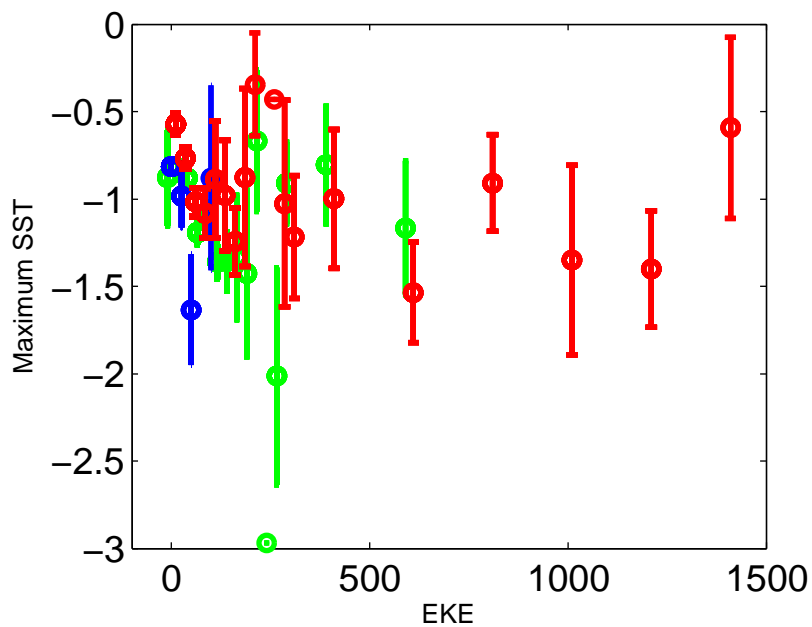
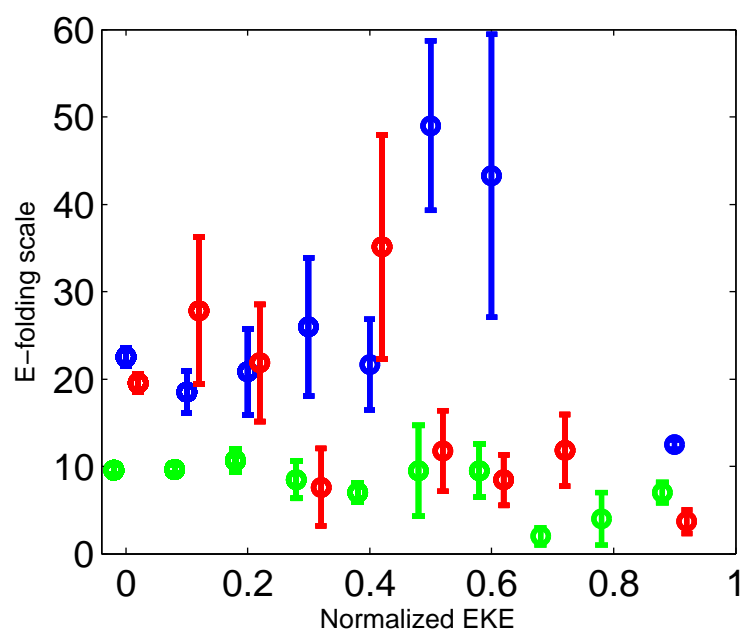
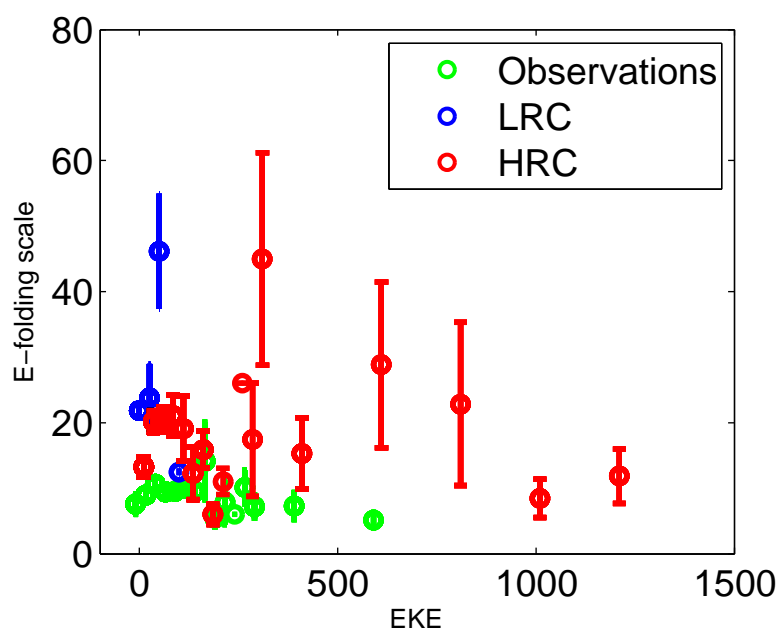


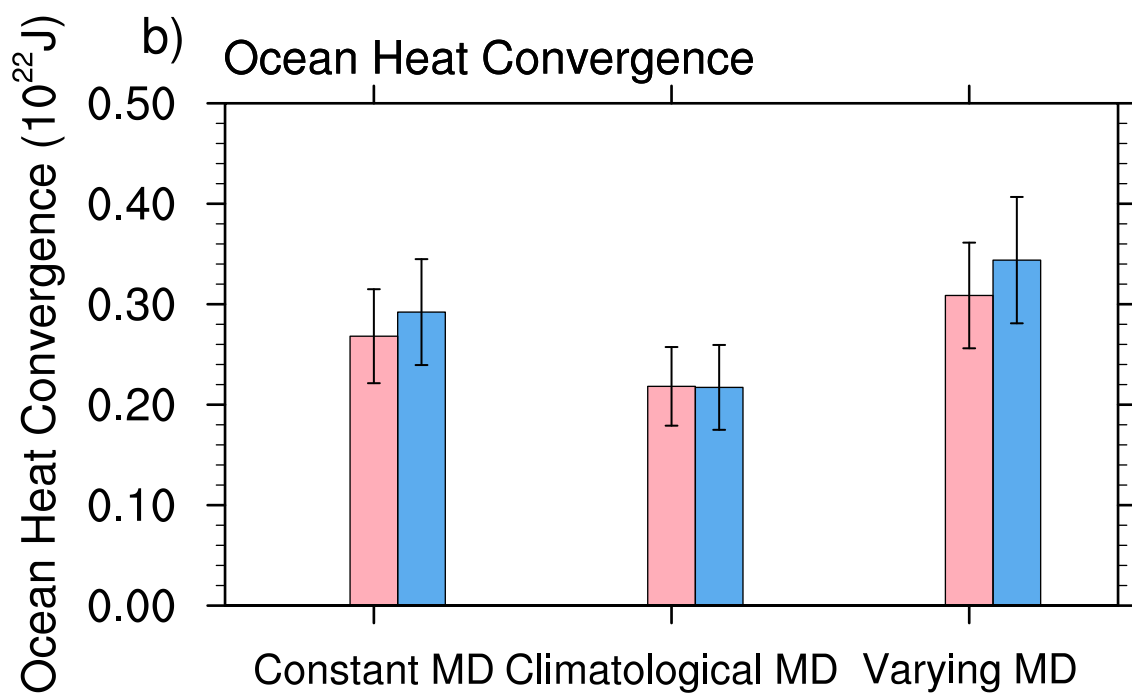
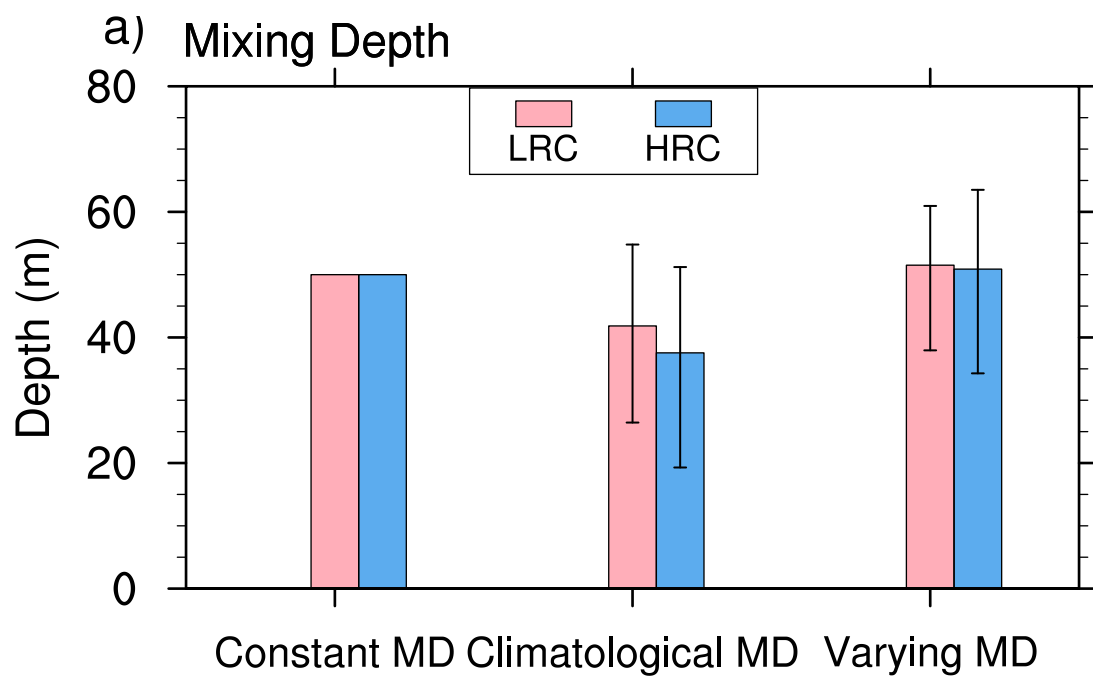


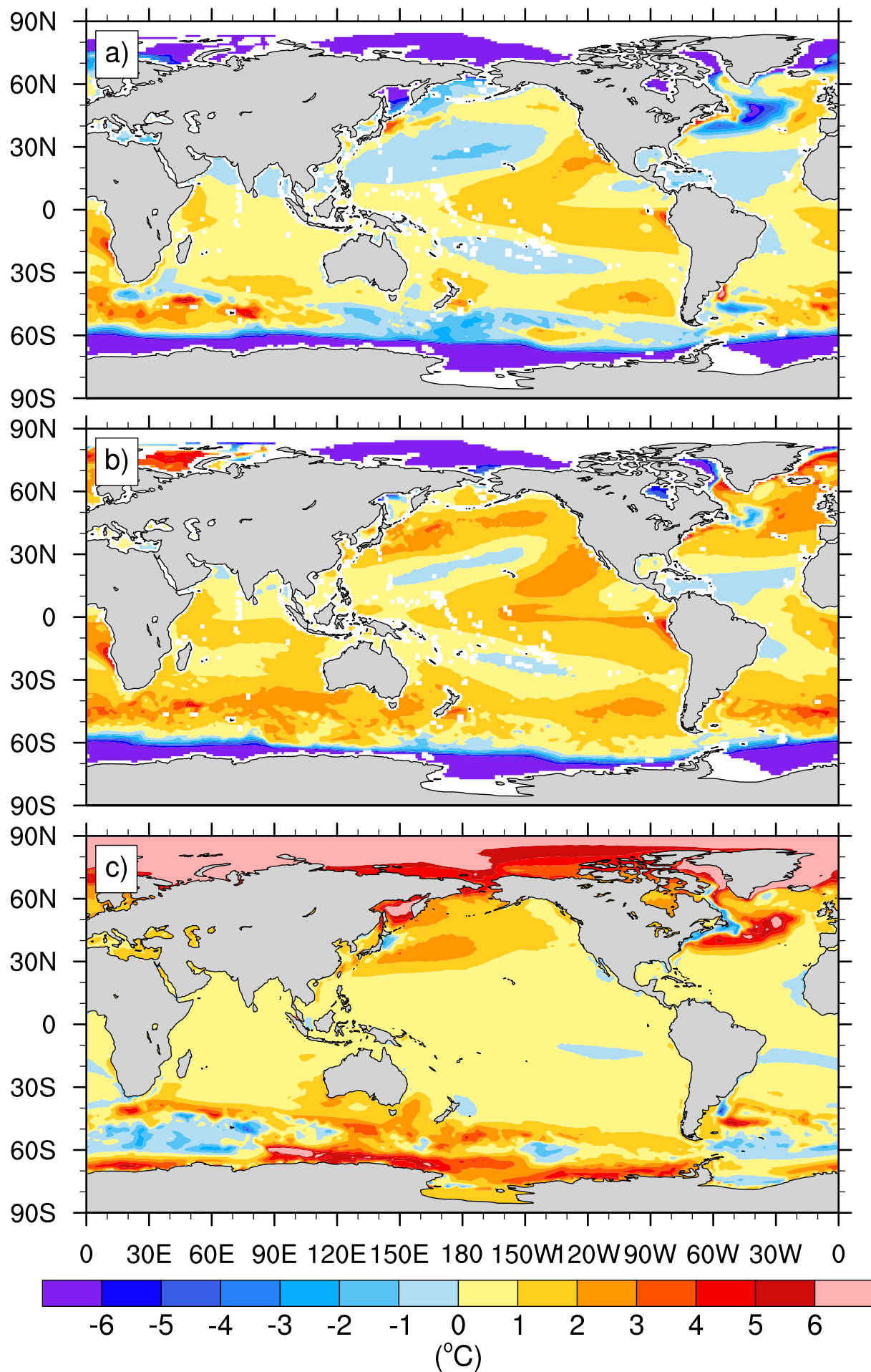


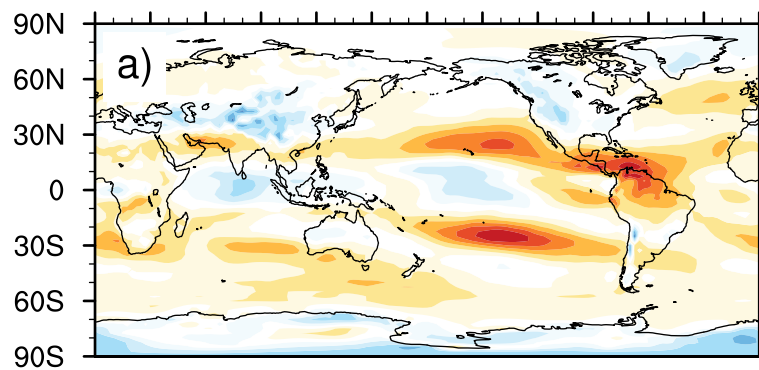
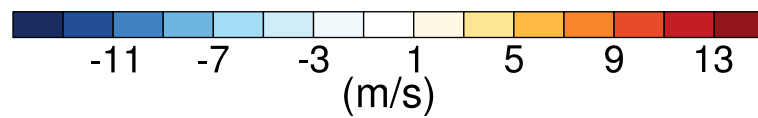
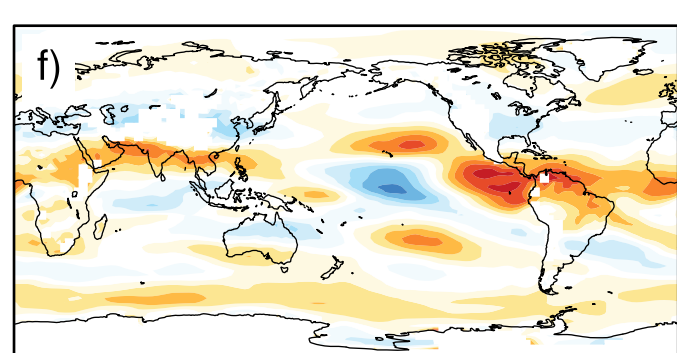
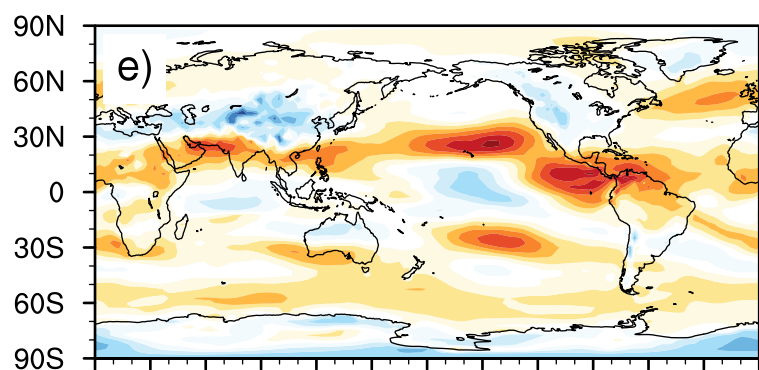
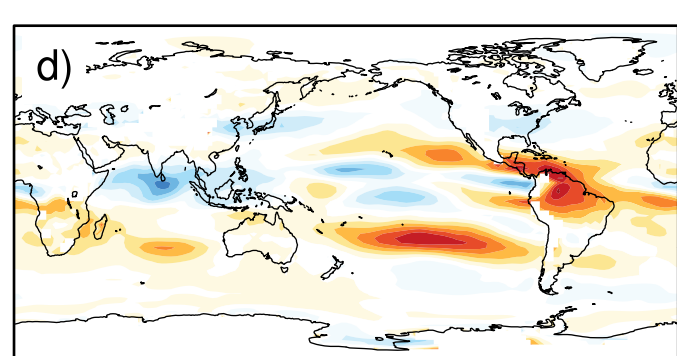
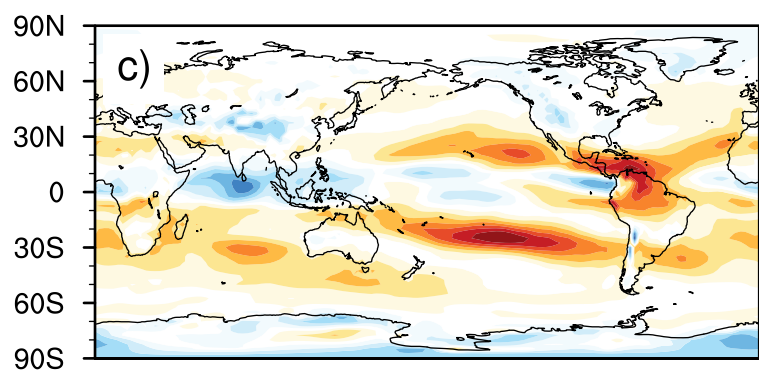
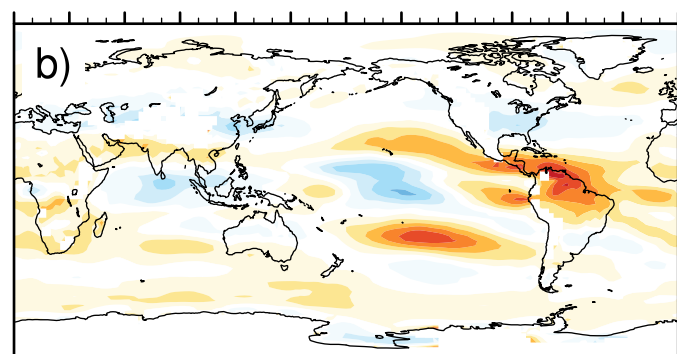




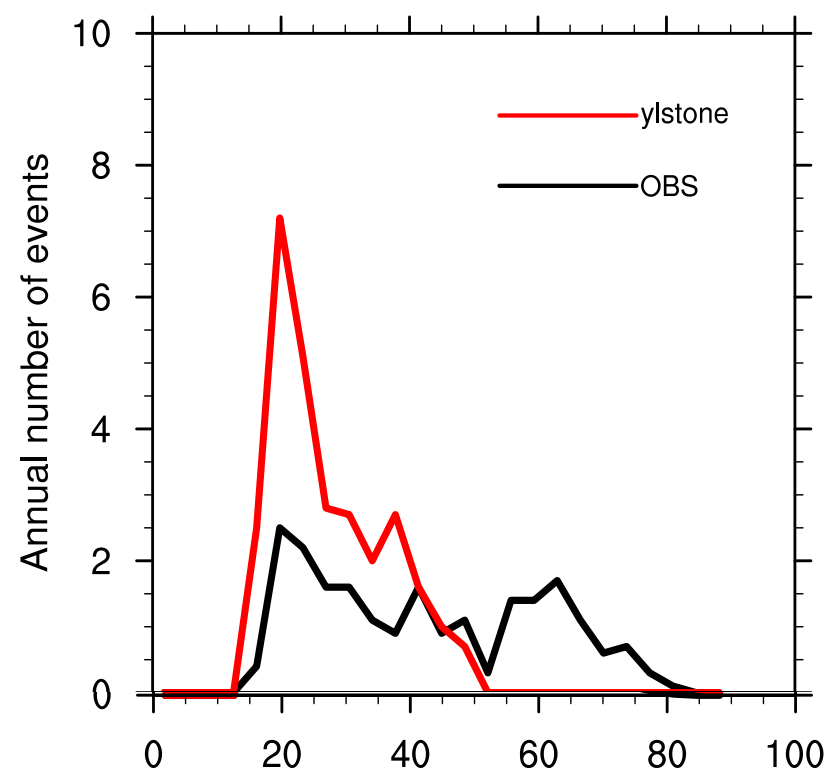




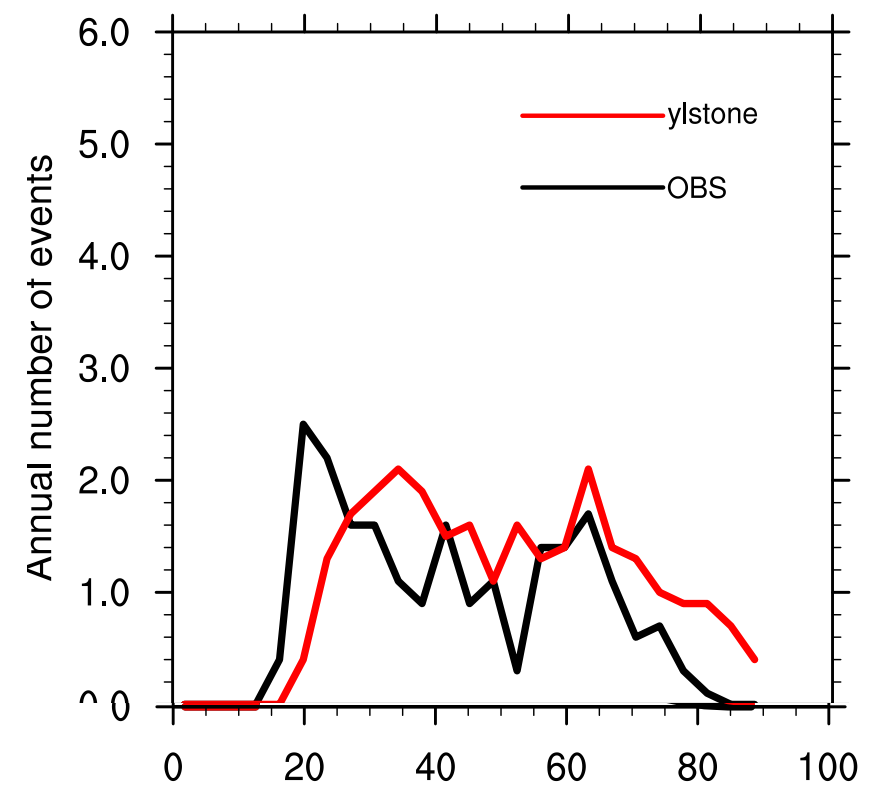


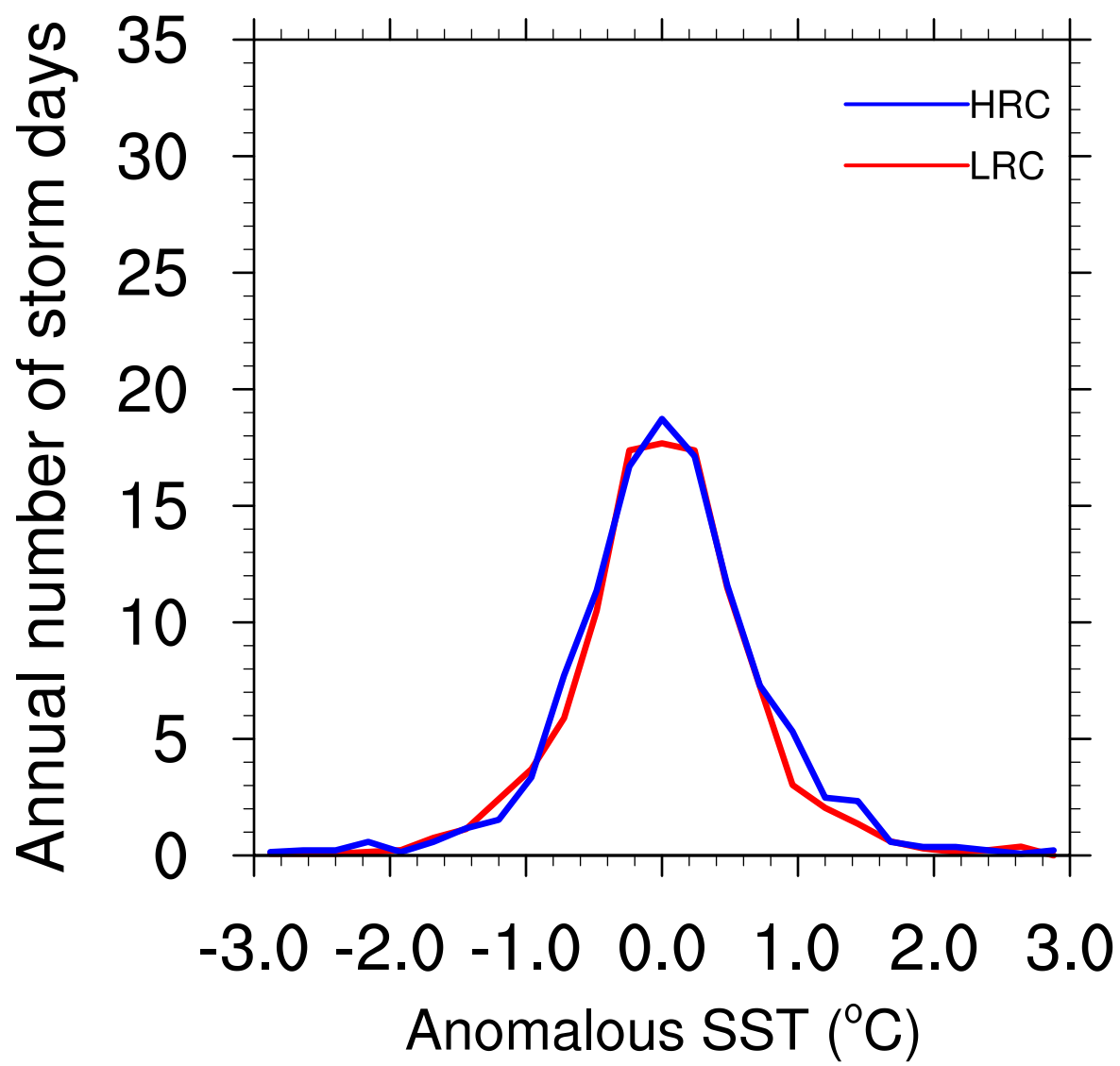
LRC-OBS**HRC-OBS**

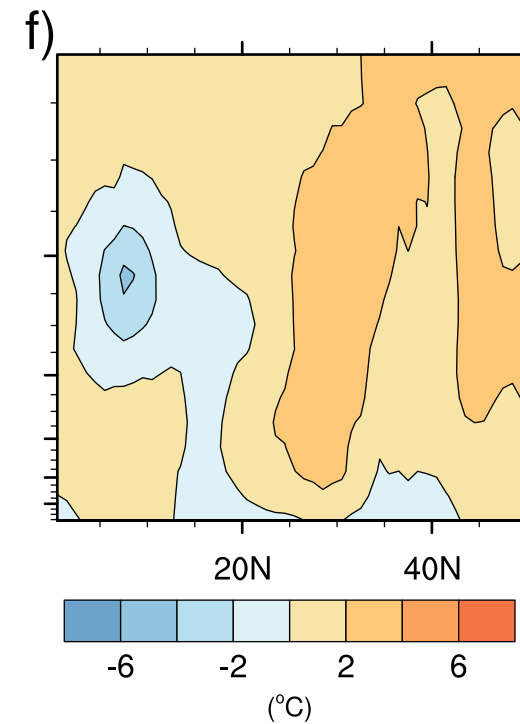
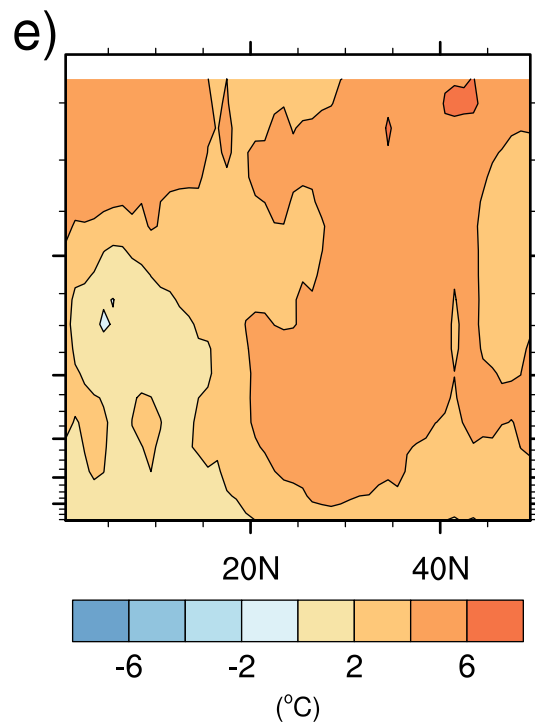
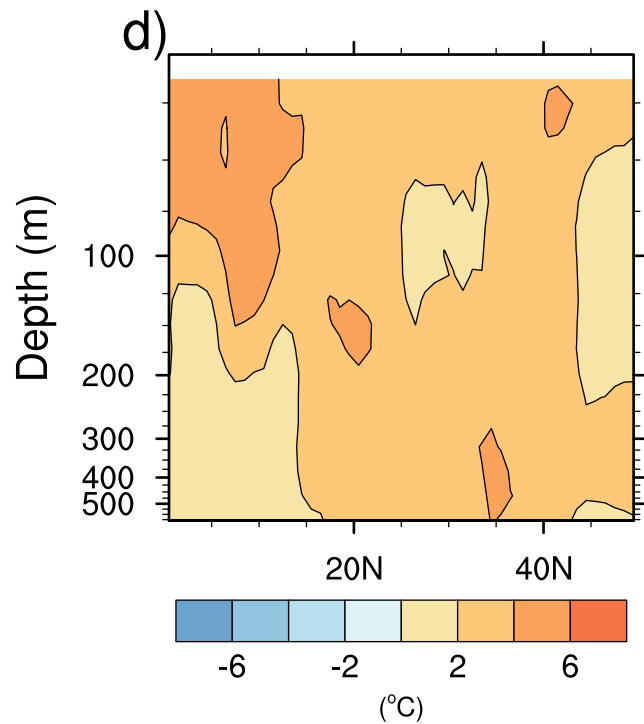
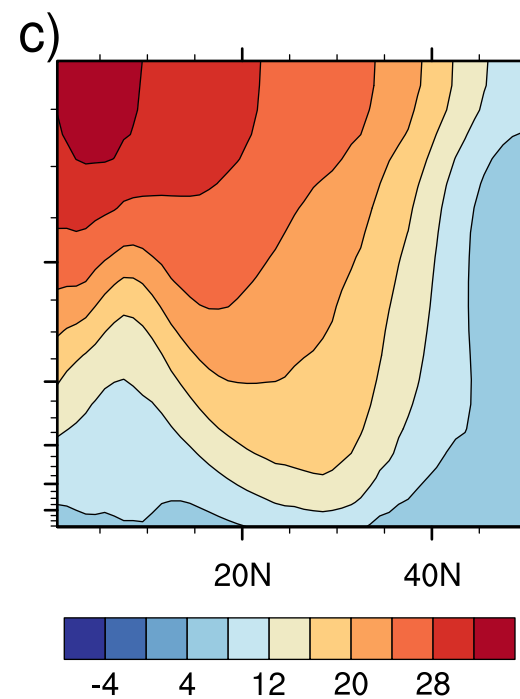
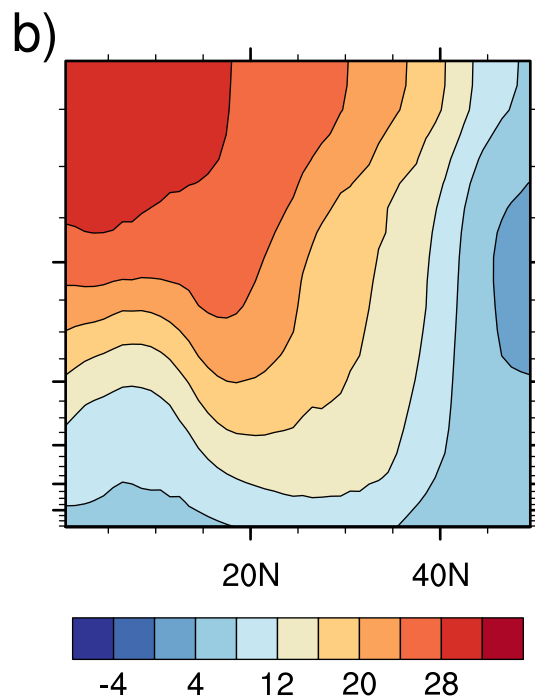
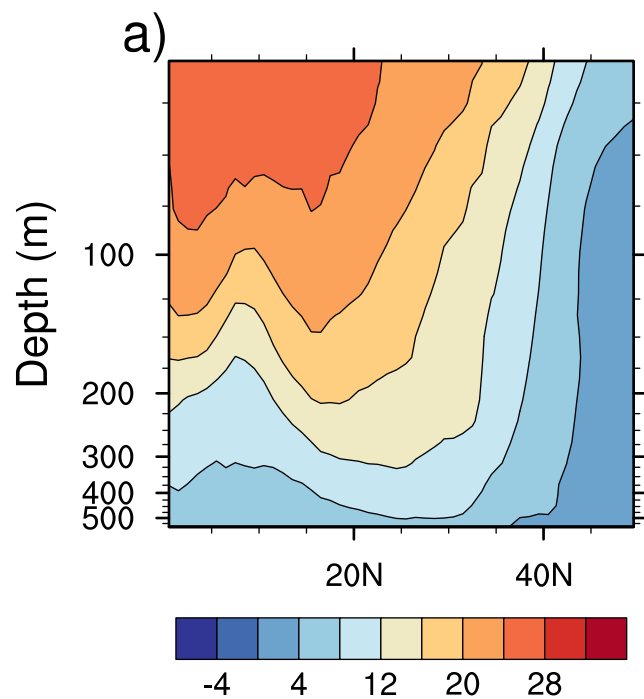
0.25 degree, daily



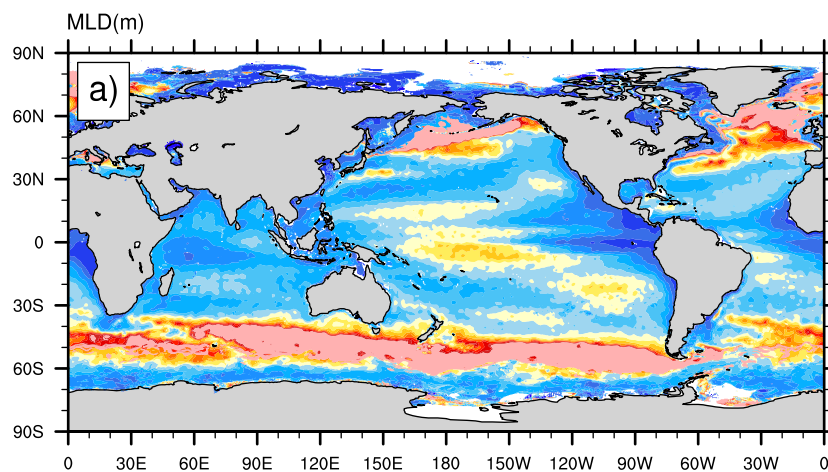
0.25 degree, 6 hourly



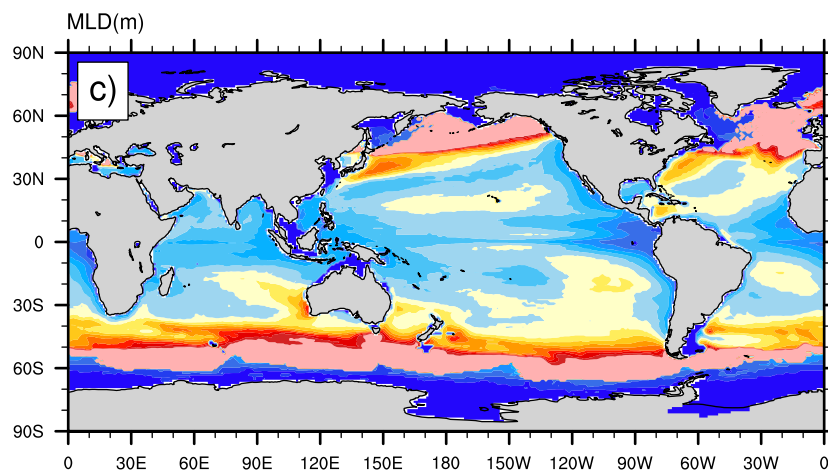




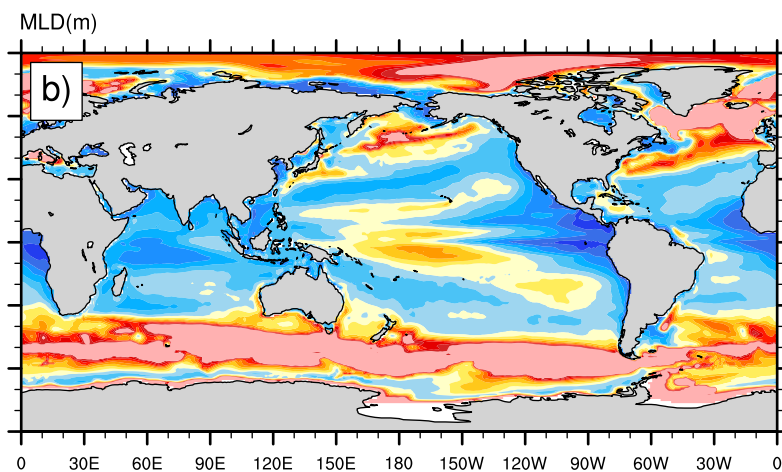
WOA13



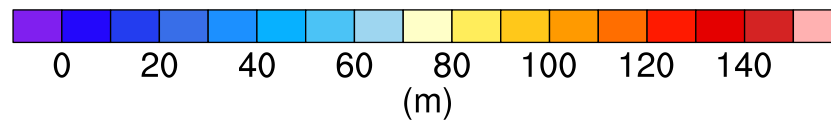
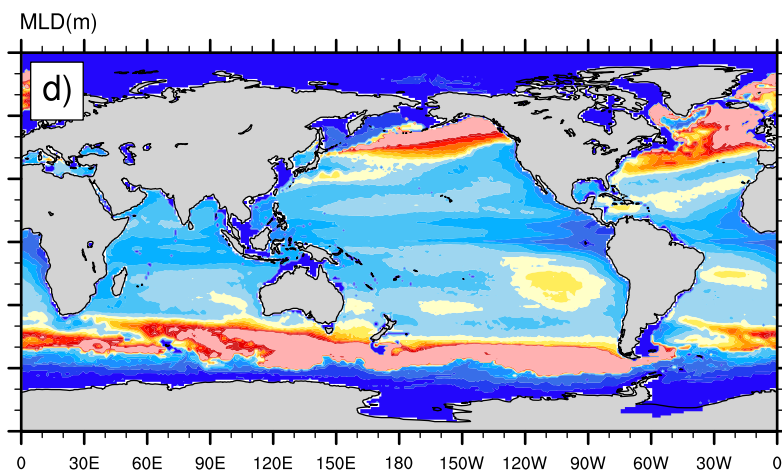
LRC



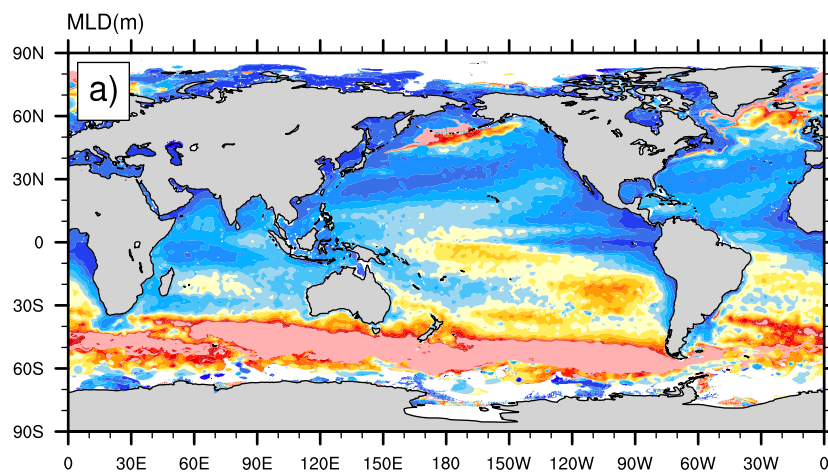
ECMWF



HRC

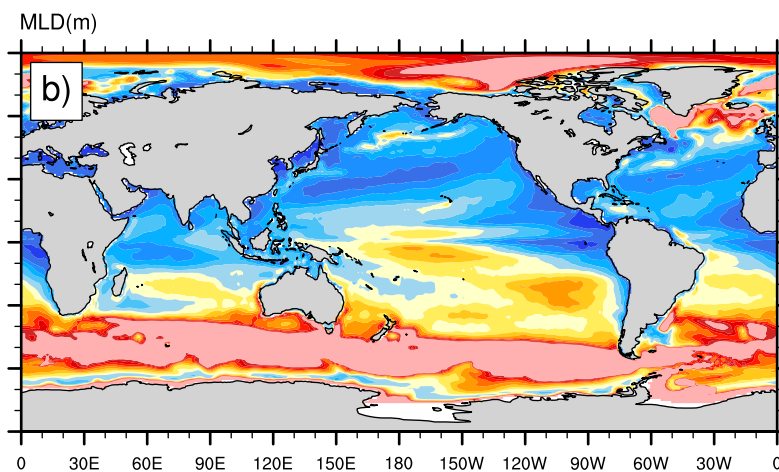


WOA13

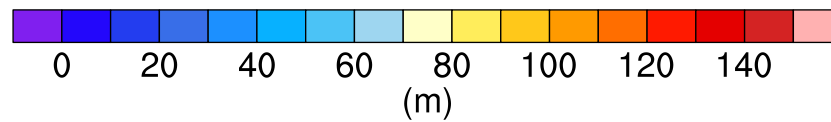
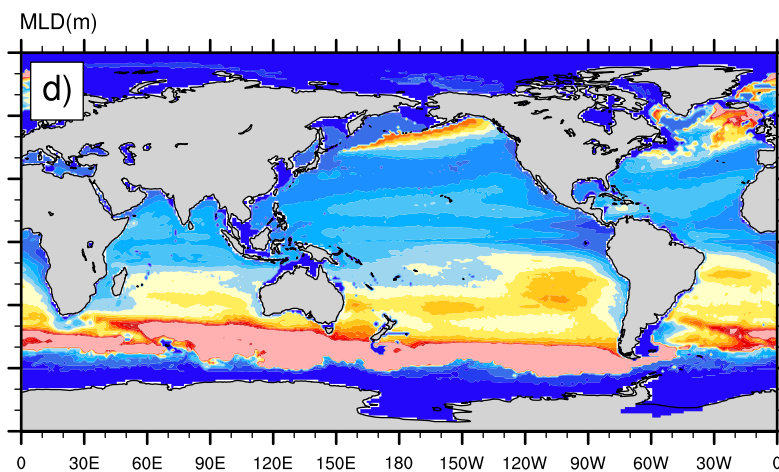
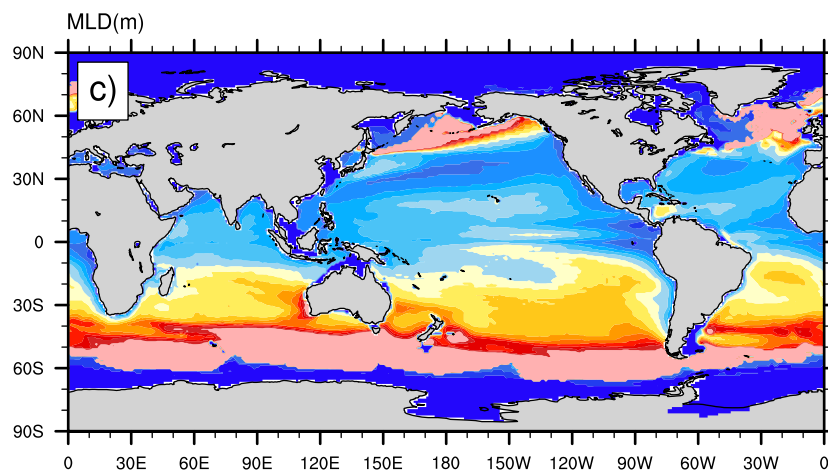


LRC

ECMWF

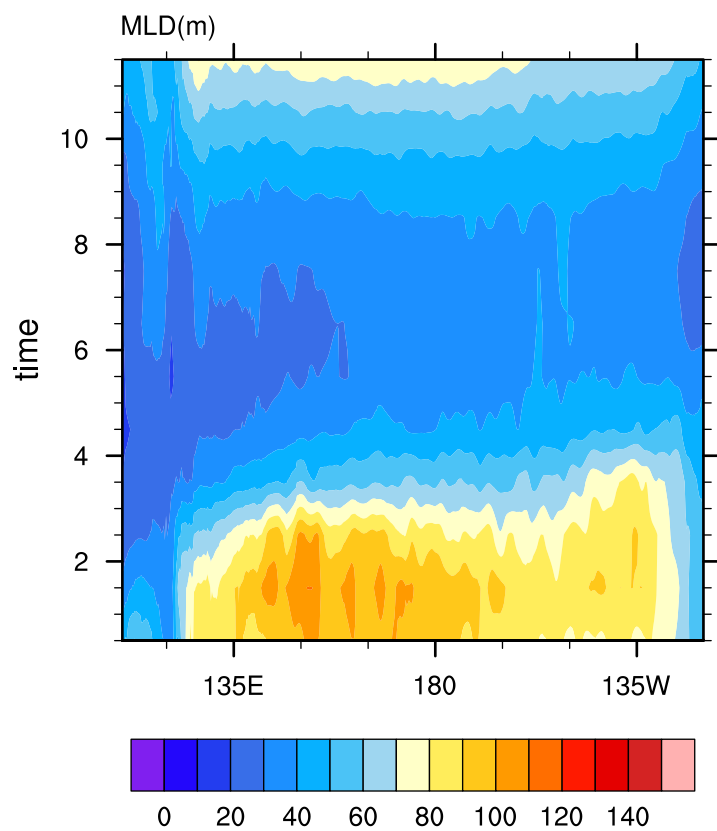


HRC

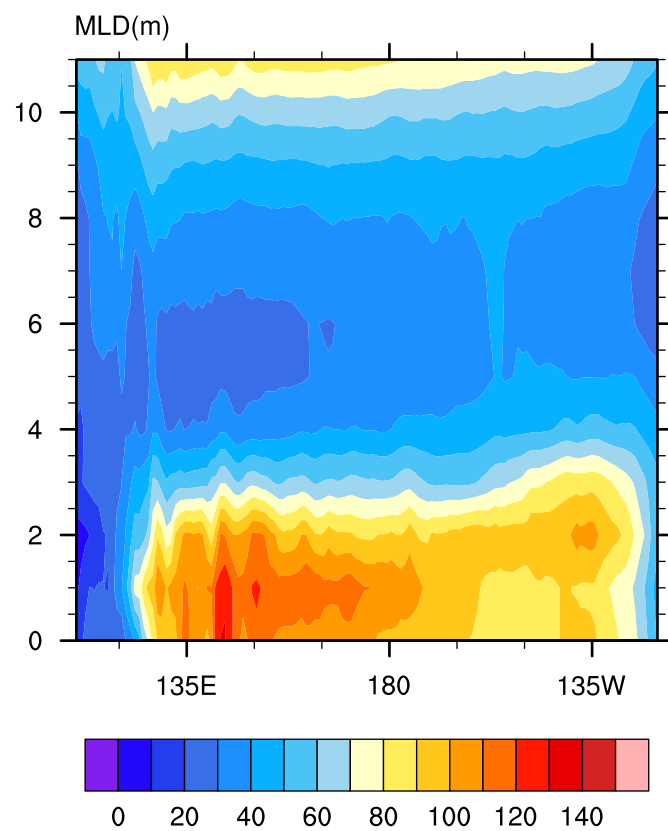


Averaged MLD between 10N - 40N

WOA13



ECMWF



Averaged SST between 10N - 40N

WOA13

ECMWF

